# Universiteit Antwerpen

## This item is the archived peer-reviewed author-version of:

Computational fluid dynamics-assisted process intensification study for biomass fast pyrolysis in a gas-solid vortex reactor

## Biofuels and Biomass

# CFD-assisted Process Intensification Study for Biomass Fast Pyrolysis in a Gas-Solid Vortex Reactor

Shekhar R. Kulkarni, Laurien Vandewalle, Arturo Gonzalez Quiroga, Patrice Perreault, Geraldine J. Heynderickx, Kevin Marcel Van Geem, and Guy B Marin

## Just Accepted

1      CFD-assisted Process Intensification Study for Biomass Fast Pyrolysis in a Gas-

2      Solid Vortex Reactor

3      Shekhar R. Kulkarni[1], Laurien A. Vandewalle[1], Arturo Gonzalez-Quiroga[1], Patrice Perreault[2],

4      Geraldine J. Heynderickx[1], Kevin Van Geem[1] and Guy B. Marin[1]

5      [1] Laboratory for Chemical Technology, Ghent University, Ghent, Belgium

6      [2] Universidad Autónoma de Yucatán, Calle 60 491A, Centro, 97000 Mérida, Yuc., Mexico

7

8      Abstract

9

10      The process intensification possibilities of a gas-solid vortex reactor have been studied for

11      biomass fast pyrolysis using a combination of experiments (Particle Image Velocimetry) and

12      non-reactive and reactive 3D CFD simulations. High centrifugal forces (greater than 30 g's) are

13      obtainable, which allows for much higher slip velocities (> 5 m s$^{-1}$) and more intense heat and

14      mass transfer between phases, which could result in higher selectivities of for example bio-oil

15      production. Additionally, the dense yet fluid nature of the bed allows for a relatively small

16      pressure drop across the bed (~$10^4$ Pa). For the reactive simulations bio-oil yields of up to 70 wt.

17      % are achieved which is higher than reported in conventional fluidized beds across the literature.

18      Convective heat transfer coefficients between gas-solid in the range of 600 - 700 W m$^{-2}$ K$^{-1}$ are

19      observed, significantly higher than those obtained in competitive reactor technologies. This is

20      partly explained by reducing undesirable gas-char contact times due to preferred segregation of

21      unwanted char particles towards the exhaust. Experimentally, systematic char entrainment under

22      simultaneous biomass-char operation suggested possible process intensification and a so-called

23      "self-cleaning" tendency of vortex reactors.

1  Keywords: Biomass Fast pyrolysis, CFD, Process Intensification, Vortex Technology, Detailed

2  Kinetics

## 1. Introduction

5  With global energy demands increasing and increased concerns about climate change and

6  depleting resources for fossil fuels, the share of energy and fuel demands met by renewable

7  resources should be increased. For that, several energy-providing alternatives are to be upgraded

8  over the coming years, spanning from renewable energies like solar, wind, geothermal, etc. to

9  nuclear and hybrid electric technologies [1, 2]. Biomass fast pyrolysis however possesses a unique

10  advantage of simultaneously producing energy as well as fuel and chemicals. Biomass fast

11  pyrolysis refers to the conversion of biomass to bio-oil, in the absence of oxygen, and in the

12  temperature range of 773 to 873 K. With appropriate downstream processing, the liquid product,

13  referred to as bio-oil, can replace conventional fossil fuels upon subsequent stabilization[3, 4]. Bio-

14  oil is a mixture of over hundreds of aromatic compounds, ranging from simple aldehydes, acids,

15  ketones to complex poly-aromatic hydrocarbons (PAHs) and various oxygenated aromatics[5, 6].

16  Next to these groups of chemical compounds, bio-oil is also rich in high-valued chemicals, e.g. 4-

17  ethylguaiacol, furfural, creosol (or 4-methyl-guaiacol) and catechol. Separation of the latter,

18  though not trivial, offers additional economic incentives to study biomass fast pyrolysis[7].

19  Experimental, computational and modeling studies on biomass fast pyrolysis have been reported

20  over the past few decades[8], with most of the research focusing on developing technologies to

21  maximize bio-oil yields from a variety of biomass feedstocks[9-12].

22  Computational fluid dynamics (CFD) has been proven an efficient tool to simulate gas-solid

23  hydrodynamics in various reactor technologies, coupled with different reaction kinetics[13-18], of

1    different complexity [19]. This has motivated an increasing interest in CFD studies for reactor

2    optimization and design for biomass fast pyrolysis and related processes. Usually, CFD studies

3    are explorative in nature, which implies that experimental data are needed to validate the applied

4    models. Furthermore, due to the immense potential of these CFD tools, they are sometimes used

5    as a predictive tool, e.g. either when it is too costly to perform the experiments or the data is

6    scanty. Both Euler-Euler and Euler–Lagrange CFD models have been used in biomass fast

7    pyrolysis numerical studies. In the Euler–Euler approach, the gas phase and the solid phase are

8    treated as continuous, interpenetrating phases. In the Euler–Lagrange model, on the other hand,

9    the gas is treated as a continuous phase while the solid particles are treated as a discrete phase,

10   allowing one to study the various solid-fluid-wall interactions in detail. Due to ease of application

11   and the ability to handle larger-scale systems, most of the CFD studies on biomass fast pyrolysis

12   in the literature rely on Euler-Euler modeling approach. Euler-Lagrange modeling approaches

13   resolve intra-particle interactions like thermochemical degradation, shrinkage, breakage,

14   segregation, mixing, etc. resulting in intensive computational costs[20].

15   The choice of the solution domain, i.e. two-(2D) or three-dimensional (3D) often appears to be a

16   distinguishing factor in CFD studies. It has been pointed out that the bed hydrodynamics can vary

17   significantly when obtained using a 2D or a 3D approach[21]. For e.g., a study[24] indicated 3-D

18   bubbling fluidized bed reactors predict faster bubbles formation compared to a 2D case, as a

19   reason of reduced drag force. However, some studies have also shown the 2D geometries being

20   adequate to satisfactorily mimic the behavior of a 3D simulation domain result as well as the

21   experimental data under consideration[22-24].

22   From the point of view of the reactive Euler-Euler simulations, the computational cost of

23   simulations mainly depends on the level of details in the kinetic model chosen, other than the

1   choice of the computational domain. Three main groups of biomass fast pyrolysis kinetic models

2   can be distinguished in that regard: Single-Component models, Multi-Component simple models

3   and Multi-Component detailed models. In the single-component (or lumped) models biomass

4   decomposes into gas, tar (bio-oil) and char. Often, intra-product reactions with secondary

5   degradation reactions of tar are included [25-28]. On the other hand, multi-component models study

6   biomass degradation via its constituent components: cellulose, hemicellulose and lignin, each

7   with an appropriate mass fraction. Often a fourth component, water, is also considered. Cellulose,

8   hemicellulose and lignin are converted into their activated intermediate forms which then further

9   decompose into gas, tar and char. Tar is considered to undergo secondary cracking reactions

10  forming gas as well[29]. Finally, the most comprehensive models assume that biomass is composed

11  of cellulose, hemicellulose and three types of lignin[30]. The activated forms of cellulose and

12  hemicellulose, which are often referred to as the transient liquid state[31], react to form different

13  organic molecules, instead of being lumped into gas, tar and char. It was found that the best

14  predictions are made by the detailed models, with the product yields being largely controlled by

15  rapid biomass devolatilization, however at a substantially larger computational cost[32]. It was also

16  found that the reactor hydrodynamics, temperature and biomass volume fraction are not affected

17  by the specifics of the applied kinetic model [29].

18  Conventionally fluidized bed reactors are used for studying biomass fast pyrolysis in chemical

19  engineering research[33, 34]. Simplicity in design and operation, ease of handling two-phase flows,

20  and absence of moving reactor parts are some of their attributes making them popular, not only

21  for biomass fast pyrolysis studies, but for industrial applications as well[35]. Despite these

22  advantages, fluidized beds possess some inherent design drawbacks: limitation on the usable gas

23  flow window from minimum fluidization to bed entrainment, and mostly a non-isothermal solid

1     bed due to limited heat and mass transfer[7]. Especially this last drawback restricts the fluidized

2     bed reactor technology from being ideal for thermally intensive processes like biomass fast

3     pyrolysis. For e.g., the maximum bio-oil yield in fluidized bed reactors is reported to be ~66-68

4     % while operating at 773 K[36].

5     The moderate interphase contact can be overcome, whilst retaining the benefits of the fluidized

6     bed reactor technology, by replacing the gravitational force by a centrifugal force[37]. Gas-Solid

7     Vortex Reactors (GSVRs) are a new generation of centrifugally fluidized bed reactors in a static

8     geometry with the centrifugal force generation achieved via gas throttling through small,

9     azimuthally inclined openings, called slots[38]. Operating in a centrifugal field results is an

10    increased radial packing of solid bed, a higher gas-solid slip velocity and a shorter gas residence

11    time, owing to the high gas flow rates. Preliminary studies in literature illustrate that vortex

12    reactors might be usable for studying/executing various multiphase processes like drying[39, 40],

13    biomass fast pyrolysis[41]; $SO_2$-$NO_X$ absorption[42], etc. However, to maximize the other benefits

14    from these reactors like particle-particle segregation[43, 44], optimizing process conditions to

15    maximize yield of desired compounds, various level of optimization studies still need to be

16    performed. Reactor geometry, slot size-shape, continuous solid feeding and removal facilities

17    with various outlet configuration[45], etc. are few worth mentioning.

18    At the Laboratory for Chemical Technology (LCT, Ghent University) experimental and

19    numerical vortex technology research has evolved from single phase to gas-solid hydrodynamics

20    studies[46-49]. Preliminary numerical studies have resulted in assessing the capabilities of the vortex

21    reactor technology for process intensification of various chemical engineering processes,

22    including biomass fast pyrolysis[41, 42]. Recently, using in-house and literature-obtained

23    experimental data, a drag law was proposed for a vortex reactor[50] in order to capture drag more

5

1 accurately in the vortex reactors. . One of the most promising chemical processes in the GSVR is

2 biomass fast pyrolysis. In the present study, 3-D reactive CFD modeling is used to study the

3 process intensification desirable for biomass fast pyrolysis in this vortex reactor using a detailed

4 fast pyrolysis reaction network and to evaluate/optimize the reactor design. Previous work[44] from

5 LCT made use of a lumped kinetic model for biomass degradation, which raises questions about

6 the accuracy of the obtained results. Moreover, this does not allow to evaluate the potential of the

7 GSVR for chemicals production because individual yields could not be tracked. Moreover in this

8 work use is made of 3-D simulations as compared to 2-D by the authors[44]. This choice of 3-D

9 simulation domain allowed to closely capture the solid to end wall effects in this reactor; which

10 are substantial. Therefore first the CFD model is validated using novel experimental data using

11 ideal spherical particles. The validated model is then used to study various non-reactive biomass-

12 char and reactive biomass fast pyrolysis simulations in this reactor.

13 2. GSVR Experimental Setup

14

15 The GSVR experimental set-up used in the present study is described in detail by Gonzalez-

16 Quiroga et al.[51]. Fig. 1 shows the top and front views of the GSVR. Compressed air is used here

17 as the fluidizing agent. It enters tangentially in the gas inlet jacket of diameter 0.125 m.

18 Thereafter, the air is distributed in the cylindrical GSVR chamber via eight equi-spaced,

19 tangentially oriented inlet slots of 1 mm width each. On the other hand, solid (aluminum for CFD

20 validation experiments and biomass, char for the others) particles enter the reactor chamber

21 through a 1.5 mm diameter conduit on the top plate. A compressed air line operating at a

22 negligible gas flow rate (compared to the main gas) assists in this pneumatic conveying of solid

23 into the reactor. To avoid disturbances in operation, this additional air is fed at slightly higher

1 pressure than those existing inside the reactor. Solids enter the chamber at a radial position of 36

2 mm.

3 A typical experimental procedure in the reactor is as follows. Gas flow is established in the

4 reactor until constant pressures are achieved across the reactor; as monitored via various pressure

5 sensors. Solids are then introduced using a slightly higher pressure on the purge air-line

6 (typically, 20-30 g). The solids addition is almost instantaneous. Excess solids entrain with the

7 exiting air and are collected in a bag filter installed downstream of the reactor. Remaining solids

8 in the reactor correspond to the solids loading of the reactor.

9 2D PIV data was acquired for a stable solids bed . The solids velocity fields were recorded with a

10 2D PIV set-up from LaVision®. Double-pulsed diffused laser light (135 mJ, 15 Hz, Nd:YAG

11 Litron laser) was used to illuminate the solids bed. A charge coupled device (CCD) camera of 4

12 megapixels (Imager-ProX4M) was set perpendicular to the bottom end wall of the GSVR in front

13 of the test section. This 2D PIV setup was controlled by LaVision DaVis software 8.1.6. Further

14 details on the application of the 2D PIV technique in the GSVR are given by Kovacevic et al.[52]

15 For each experiment, 350 pairs of images are recorded. The software is further used to export one

16 text file per each pair of images. One such file contains data on spatial coordinates and respective

17 solids velocity components. An in-house developed Python code is further employed to calculate

18 the azimuthal velocities of aluminum particles reported. Overview of PIV setup and brief data

19 processing procedure is summarized in Fig. 2.

20 3. Numerical Model

21

22 CFD model

23

1    All the simulations presented in this study, non-reactive as well as reactive, are performed using

2    ANSYS Fluent v15. The simulations are Eulerian-Eulerian in nature with gas being the primary

3    phase (compressed air for non-reactive simulations and hot nitrogen for the reactive ones), while

4    two lumped species, biomass and char, constitute the secondary phases. Inside the vortex reactor

5    the gas-solid flow is turbulent. In the present study, the turbulence is modeled with the k-ω

6    turbulence model[53]. For convenience of modeling, biomass and char particles are assumed to be

7    spherical in shape.. The solid phase is modeled using the Kinetic Theory of Granular Flow

8    (KTGF)[54, 55]. The set of conservation equations to be solved are listed in Table 1, while the

9    various constitutive equations are described in Table 2.

10   From a purely computational point of view, simulating a complete GSVR is time-consuming.

11   Simulating a sectional (or pie) geometry is less computationally intensive and is acceptable,

12   provided that all flow features captured are similar to those captured when simulating a full-

13   geometry. Our previous work has confirmed the latter[46]. In this study, a 45° pie-geometry, with a

14   gas inlet slot in the middle of the pie, as shown in Fig. 3, is used. A mesh selectivity study is

15   performed using four meshes, with a number of triangular cells of approximately 33,000; 65,000;

16   125,000 and 250,000. Since it is observed that the mesh with 65,000 cells captures the vortex

17   reactor hydrodynamics, it is chosen to perform all the GSVR simulations. All the meshes are

18   generated using Pointwise V17.

19   Biomass fast pyrolysis kinetic model
20

21   A Multi-Component Multi-Step model, as proposed by Ranzi et al.[56] is applied. The biomass

22   thermal degradation is studied in terms of individual component reactions. The reactions and

23   corresponding kinetic parameters are listed up in Table 3. Cellulose, hemicellulose and lignin

24   react into their respective products to form gas, bio-oil vapors and char. Each of these reactions

1    are assumed to be first order and irreversible. Cellulose, which is a straight-chain polymer of

2    glucosidic monomers, reacts to various products with levoglucosan being the major one.

3    Hemicellulose, approximated as a xylose polymer in this model, reacts via two intermediate

4    species: HCell 1 and HCell 2. This decomposition leads to the release of various product gases,

5    due to reactions as well as to the release of interstitially present ones.  Lignin has a complex

6    aromatic matrix structure which needs to be identified using three model compounds:  LignC,

7    LignO, LignH, rich in carbon, oxygen and hydrogen, respectively, and based around a common

8    $\beta$-O-4 aromatic skeleton.

9    4. Model Validation

10

11   To demonstrate the capabilities of the GSVR technology for biomass fast pyrolysis, the

12   numerical model needs to be validated. Therefore the CFD model for non-reactive reactor

13   hydrodynamics is validated using in-house gathered non-reactive experimental data in the GSVR

14   geometry as described above.

15   Cold-flow experiments for air-Aluminum two-phase flow are performed in the vortex setup. The

16   geometrical and operating conditions are listed up in Table 4. During experiments, for a stable

17   flow configuration, solid azimuthal velocities are recorded using particle image velocimetry

18   (PIV). For a discussion of PIV measurements reference is made to our previous work[51]. The PIV

19   velocity data is used for validating non-reactive CFD simulation results.

20    For simulations. the solids are fed in the vortex reactor by defining a User Defined Function

21   (UDF) in ANSYS Fluent v.15, which allows feeding Aluminum particles in the radial zone of

22   0.038 m < r < 0.039 m. Other operating conditions for these simulations are specified in Table 4.

1  Simulations indicate the formation of a moderately packed Aluminum bed with a height of ~8

2  mm as seen in Fig. 4. The solid volume fraction profile is displayed in the mid-section angular

3  plane, passing through the middle of the slot in the computational domain. This simulation result

4  gives a qualitative match with the visually observed experimental bed height.

5  PIV data, indicates the particle azimuthal velocity component to be an order of magnitude higher

6  than the radial component, confirming the rotational nature of the solid bed. As seen in Fig. 5 (a),

7  the azimuthal velocities vary between 0.5 and 4 m s$^{-1}$ with the velocity being the highest in

8  between two slots. The radial component of the solid velocity is observed to be between -0.3 to

9  0.3 m s$^{-1}$ , i.e. on average 0 m s$^{-1}$. (not shown). The most effective momentum transfer from gas

10  to particles is realized in the very first layer of the bed (r = 39 mm), at the circumferential wall,

11  where the azimuthal velocity reaches its highest values. Subsequent reduction in radius sees the

12  effective momentum transfer reducing, resulting in diminishing bed velocity, as indicated in Fig.

13  5 (b) & (c). All the azimuthal velocities from the simulations to be compared with the PIV data

14  are sampled in the solid bed, on the bottom plate, at an axial location of z=0 mm

15  A comparison of experimentally recorded and simulated pressure drop data is presented in Fig. 6.

16  The pressures are reported with respect to the outlet pressures for the respective case. The data is

17  compared at 7 different locations across the reactor; with probes mounted at the positions enlisted

18  in Table 5.

19  Fig. 6 shows that the experimentally observed pressure drop trends are well-captured by the

20  simulations. Although the absolute pressure values differ at specified locations, the trend in

21  pressure drop is captured accurately. As can be seen, the major contributor to the pressure drop is

22  at the slots. Rapid compression and expansion of gas, throttled at high velocity though small slot

23  openings results in these high pressure drops.

1 These pressure and velocity comparisons between experiments and simulations show good

2 qualitative and quantitative agreements. As such, the CFD model used is validated based on air-

3 Aluminum experimental data obtained in the vortex reactor studied. The numerical model will be

4 used for further (non-) reactive simulations of the GSVR.

5 Finally, in order to validate the reactive UDF used for this work, simulations have been

6 performed on a Drop Tube Reactor (DTR) using the same UDF and compared with the

7 experimental data provided by Guizani et al.[57]. Details and results are provided in Supporting

8 Information.

## 5. Results and Discussion

10

11 With the numerical reactor model validated, a parametric study of the GSVR has been performed.

12 In a first step, non-reactive simulations of the GSVR are performed to evaluate the effect of

13 particle diameter, solid loading and feed temperature on the GSVR hydrodynamics. The two

14 secondary solid phases considered in the present study are biomass and char. Distinguishing

15 between biomass and char allows to study their mutual interaction as well as in their interaction

16 with gas and reactor walls, independently. Continuous release of products from a reacting

17 biomass particle results in its shrinkage. The remainder of the biomass particle, mainly a carbon

18 residue with traces of metals and minerals, is referred to as char. Thus, char diameters are smaller

19 than those of the original biomass particles. Due to the presence of heavy, metallic residues in the

20 smaller char volume, char density is typically lower than, but still close to, that of biomass[58].

21 In a second step, biomass fast pyrolysis reactive simulations are performed to estimate the effect

22 of gas feed rate, gas inlet temperature, biomass feed mode, etc. Interactions of the phases with

23 each other as well as with the reactor walls are visualized in Fig. 7.

## 5.1  Biomass-Char non-reactive experiments

Solids consisted of pinewood and char originated from pinewood gasification. The average particle density and the maximum dimension of pinewood are 500 kg m$^{-3}$ and 1.5 mm, respectively[51]. The char density varies between 500 kg m$^{-3}$ for larger particles to $1621 \pm 42$ kg m$^{-3}$ for superfine char powder. The air mass flow rate was set at 12 g s$^{-1}$, which corresponds to an air injection velocity of 82 m s$^{-1}$. A rotating solids bed of pure char was generated by feeding 10 g of pure char into the GSVR chamber. After 20 s, 2 g of pinewood was added to the rotating bed. The solids azimuthal velocities corresponds to mixtures of pinewood and char measured at 1, 9 and 18 s after feeding pinewood. Azimuthal velocities shown in Fig. 8 correspond to the mean values, calculated from five 2D PIV pairs, for three time instances. The azimuthal bed velocity is the highest closer to the slot outlet as maximum momentum transfer from the incoming gas takes place threat. The bed velocities at radial positions of 38 mm are practically invariant with time. However, a substantial rise in the bed velocities at r = 34 mm is observed over time. Loss of char particles from the bed over time explains this phenomena. This selective char removal with gas flow can also be observed in Fig. 9 . Over long operation times (> 200 s), the biomass bed is further retained, without any loss of material. The latter demonstrates the char entrainment while feeding a biomass-char mixture in the GSVR.

## 5.2  Non-reactive biomass-char segregation simulations

The general settings used for the non-reactive simulations are tabulated in Table 4. The simulation is performed along the following lines: a gas unsteady state simulation is performed for an initial 0.1 s of flow time. Once a stable gas flow field has developed, a mixture of char and biomass is fed to the reactor for a limited feeding time until both are at the desired amount of mass.. During a simulation, the behavior of the two secondary phases is followed until a steady

1   state is reached. Next, the time-averaged contours of various volume fractions are plotted to

2   assess (possible) biomass-char segregation. The solid bed volume fraction fields are visualized on

3   an axial plane at z = 10 mm.

4   ### 5.2.1   Effect of diameter ratio

5

6   To study the effect of the biomass to char diameter ratio ($d_r$), simulations are performed for ratios

7   of 1 and 2.5. The biomass diameter is kept constant at a value of 0.5 mm, with the char diameter

8   varying between the simulations. It is expected that during pyrolysis the diameter ratio will be in

9   this range or even larger. Density of biomass and char are kept constant at 500 and 450 kg m$^{-3}$

10  respectively[59]. The gas flow rate is set at 40 Nm$^3$ h$^{-1}$. The loading for both solid phases is kept

11  constant (20 wt. % char), implying that the number of biomass particles remains unchanged,

12  while more char particles are fed when the char diameter is smaller. In Fig. 10 (a) the biomass

13  fraction near the wall, especially in front of the injection slot, is found to be high. While, in Fig.

14  10 (b), there is hardly any char at that position. Thus, the simulations indicate that segregation

15  can be achieved. In Fig. 10 (c) and (d), the biomass and char fractions are distributed over the

16  whole solids domain, due to the fact that the density ratio of both is almost 1. It can be suggested

17  that the segregation becomes more active when the diameter ratio increases. The total solid

18  loading in the reactor during these simulations is ~6 g, while the char constitutes 40 wt. % of total

19  loading.

20  ### 5.2.2   Effect of loading ratio

21

22  To study the effect of the biomass to char loading ratio, simulations have been performed for a

23  ratio of 1.5 [Fig. 11 (a) and (b)] and a ratio of 4 [Fig. 11 (c) and (d)]. The biomass and char

24  diameters are both kept constant at values of 0.5 mm. Biomass loading in both the cases is kept

1    constant, with char loading (and thus the total solid loading to the reactor) varied. For a loading

2    ratio of 1.5, the total solids fed to the reactor is 7.1 g; while that for the loading ratio of 4, is 5.3

3    g. It is observed that varying biomass-char loading (1.5 - 4) does not affect the segregation of

4    biomass and char. It is also observed that the biomass-char mixture inside the reactor is well

5    mixed for these conditions, even at very low char loadings. The simulations thus suggest that in

6    practical operation for biomass fast pyrolysis that these feed ratios need to be avoided if the

7    desired phase segregation is to be maintained. The absence of char particles near the slot opening

8    could be resulting from their lower loading. Simulations also predict slugging solid beds for the

9    operating conditions employed.

10   ### 5.2.3    Effect of temperature

11

12   Pyrolysis temperatures vary between 600 and 800 K. As compared to room temperature

13   conditions gas velocities rise (for a fixed gas flow rate of 40 $Nm^3\,h^{-1}$) which could have an effect

14   on various interactions, and thus on bed segregation. Non- reactive simulations are performed at

15   289 K and 842 K. The biomass and char diameter has a value of 0.5 mm. The gas flow rate is 40

16   $Nm^3\,h^{-1}$. The biomass to char loading ratio is kept constant at 1.5, while the total solid loading in

17   the reactor is ~ 6g.

18   As seen in Fig. 12 , the volume fraction fields for char and biomass are barely affected by the

19   temperature. At both temperatures, a moderately packed solid bed is displayed. It can thus

20   illustrate that the hydrodynamics of biomass-char systems inside a vortex reactor is largely

21   independent of the operating temperature in the reactor. Phase interactions can thus be studied at

22   room temperature conditions, which allows reducing simulation costs by neglecting the energy

23   equations.

1   However, in continuous operation of industrial biomass fast pyrolysis reactors, char particles

2   spend only a short time in the reactor (order of a second) simultaneously with biomass particles

3   (along with rapid conversion of biomass to products). Nevertheless, the above simulation results

4   indicate the capability of the vortex reactor to simultaneously operate with multiple solid phases

5   and induce solid phase segregation if high biomass-char diameter ratios are maintained (> 2.5) or

6   if high biomass-char loading is maintained (> 60 % biomass).

7

8   ### 5.3 Reactive biomass fast pyrolysis simulations

9

10   Biomass fast pyrolysis simulations are performed to assess the process intensification of the

11   vortex reactor technology. The model used for lignocellulosic biomass thermal degradation,

12   along with the kinetic parameters for all the reactions is described in Table 3, while the biomass

13   properties and general simulation conditions are enlisted in Table *6*.

14   The biomass composition on dry weight basis is considered to be as follows: cellulose (Cell): 36

15   %, hemicellulose (HCell): 47 % and lignin (Lign): 17 %. 10 wt. % water is also considered as

16   part of biomass composition for simulation purposes. The composition is assumed to be of a

17   typical pine. Other components typically observed in the biomass like ash, extractives, etc. are

18   neglected from the composition in order to restrict the kinetic network to only primary

19   component thermal decomposition. The energy required for the endothermic fast pyrolysis is

20   provided using a hot nitrogen gas stream. The thermodynamic properties have been evaluated in

21   the range of 800-900 K. Table S 1 enlists various physical properties of the biomass constituents

22   employed for the fast pyrolysis simulations. The heat capacities and thermal conductivities for

23   the biomass species were taken from [60].

1    Instantaneous solid volume fractions for the representative base case are shown in Fig. 13 . The

2    biomass bed is observed to be densely packed with an average solids volume fraction in the range

3    of 0.4-0.42. Near the slots, the biomass bed is dilute in nature due to the injection of the gas. The

4    effect is slightly propagating within the solid bed. The char bed on the other hand, owing to the

5    smaller char particle diameter, comes under a higher drag to centrifugal force ratio which pushes

6    it largely towards the solids exhaust (c.f. section 5.3.3). The solids volume fractions inside the

7    reactor reaches values as high as 0.5, showing a densely packed biomass bed.

8    Fig. 14 displays the mass fraction fields for one of the important products of biomass fast

9    pyrolysis: phenol. Near the slot opening, as seen from both the axial and angular planes, the

10   product mass fraction is zero. This is expected as the incoming nitrogen achieves high velocities

11   coming out of the slots, pushing all the product gases and the solids away from that region as

12   seen in Fig. 14. Nitrogen, upon exiting the slots, expands into the reactor chamber. The expansion

13   is mostly azimuthal due to the slot geometry orientation. Gas velocity vectors from adjacent slots

14   thus result in the formation of a dead zone, approximately midway these slots, along the

15   circumferential wall. Mass (or volume) fractions are high in these dead zones.

16   The species considered while calculating yields of gas-phase and the bio-oil phase are:  Gas-

17   phase : Nitrogen, Hydrogen, Methane, Ethylene, Carbon dioxide and Carbon monoxide. Bio-oil :

18   Formaldehyde, Levoglucosan, Acetaldehyde, Methanol, Ethanol, Glyoxal, Xylan, Phenol,

19   Hydroxymethylfurfural (HMFU), p-coumaryl, Acetone,  Water and Formaldehyde.

20   5.3.1   Effect of gas flow rate

21

22   Nitrogen entering the reactor has two important functions to fulfill: firstly to act as a heat carrier

23   and supply necessary thermal energy for the reaction; and secondly to send the generated product

1    vapours and gases outside the reactor. Increasing gas flow rate thus has a combined effect on

2    yields. Higher flow rates result in smaller residence times in the reactor, thereby reducing

3    effective gas-solid contact time. On the other hand, reduced residence times force faster removal

4    of gaseous products. To study this effect in details, simulations are performed for a wide range of

5    operating gas flow rates between 40 and 100 $Nm^3$ $h^{-1}$. Axial and azimuthal volume fraction

6    profile for an important product-phenol are as shown in Fig. 14. Product yields for varying gas

7    flow rates are reported in Fig. 15 (a) and (b). It is anticipated that with increasing gas flow rate,

8    the effect on heat transfer coefficient and yields thereof would be positive. This however doesn't

9    appear to be the case at high flow rates, typically ~ 100 $Nm^3$ $hr^{-1}$ as seen from yields in Fig. 15.

10    The increase in yields at higher gas flow rates, wherever applicable, can be attributable to the

11    combination of higher gas-solid slip velocities and subsequent increase in inter-phase heat

12    transfer coefficient.

13    Slip velocities, commonly defined as the vector difference between gas and solid velocities, are

14    limited in Fluidized Bed Reactors to the particle terminal velocities. This shortcoming in the slip

15    velocity is overcome in vortex reactor by removing the gravity dependence on the terminal

16    velocities. Fig. 16 highlights the intensified slip velocities in the biomass bed for two operating

17    conditions. On an average, the slip-velocity magnitude is 5-10 times higher than those observed

18    in the conventional fluidized bed reactors (1-2 m $s^{-1}$).

### 5.3.2   Effect of gas feed temperature

19

20

21    The influence of nitrogen feed temperature on the yields of various products in the reactor is

22    studied by varying the temperature between 800 and 900 K. At these gas feed temperatures, a

23    reaction temperature of 700 – 800 K for biomass inside the reactor is achieved. Yields are given

24    in Fig. 15 (c) and (d). The highest bio-oil yields (72 wt. %) are observed for nitrogen entering the

1    reactor at an inlet temperature of 842 K. This heat flux is sufficient to raise the biomass bed

2    temperature to ~ 773 K. Under these process conditions, it is expected that majority of biomass

3    converts into bio-oil vapors, resulting in high yields[5]. This reasoning could also explain lower

4    yields at 900 K nitrogen feed temperature, along with higher residence time of product vapors in

5    the reactor at comparatively low nitrogen flow rate (40 $Nm^3$ $h^{-1}$). Similar bio-oil yields can be

6    attained for simulation conditions (b) and (c) in Fig. 15 . This however is not applicable for the

7    char yields, as the low gas flow in (c) results in higher residence times leading to longer gas

8    contact times in the reactor. Permanent gases yield remain majorly unaltered with changes in

9    operating conditions studied.

10    As compared to ~50-60 wt. % bio-oil yields in the conventional reactor technologies like

11    fluidized bed reactors, the simulated bio-oil yields in GSVR are observed to be ~ 70 %. The

12    yields are also higher in the GSVR when compared to the other non-conventional reactors like

13    the conical spouted beds (~ 60 wt. %) or microwave pyrolysis (~ 40 wt. %) [61]. These high yields

14    in the vortex reactors are attributable to various levels of process intensification mentioned in the

15    previous sections and which will be elaborated in the further sections.

16    5.3.3    Process Intensification in the Vortex Reactor

17

18    Heat Transfer Coefficient

19

20    High convective heat transfer coefficients (HTC) are important to maximize bio-oil yield in

21    biomass fast pyrolysis reactors. For commonly employed reactors in chemical industries, the

22    convective gas-solid heat transfer coefficients are of the order of 100 – 200 W $m^{-2}$ $K^{-1}$, as

23    demonstrated by various experimental and numerical studies [62-64]. Convective heat transfer

24    coefficients are of the order of 600 – 700 W $m^{-2}$ $K^{-1}$ (Fig. 17) for gas flow rates of 60 and 100

1   $Nm^3 h^{-1}$. The drop in HTC values near the radial position of r = 36 mm results from a combination

2   of lowered local slip velocity values and decrease in gas thermal conductivity due to lowered gas

3   temperatures from heat transfer to the biomass particles. These respectively affect the Reynolds

4   number and the Nusselt number in the Gunn correlation, resulting in reduced HTC. Slip velocity

5   indeed highly influences the heat transfer. Two levels of process intensification can thus be

6   harnessed in the vortex reactors. Firstly, the high HTC values allow to use a more compact

7   reactor and still obtain the same results as in the conventional reactors. Secondly, the prospect of

8   realizing improved heat transfer, will avoid the need for a heat carrier like sand, which is

9   appealing from an operational point of view. Fluidized bed reactors (both static and circulating)

10   often need to use sand to uniformly distribute the heat supplied by incoming gas. Higher HTC

11   values will allow to obtain a near-isothermal bed without the need for a heat carrier.

12

### Radial Product Segregation

14

15   The radial position of a particle in the GSVR is determined by the balance of centrifugal and drag

16   force. When moving towards the gas outlet, the gas velocity and thus the drag on the solid

17   particles increases. The effect of this force balance is seen in action via the velocity vector fields

18   in a GSVR as shown in Fig. 13. A biomass and a char bed are formed at different radial positions.

19   As their density ratio  is close to unity, the segregation is primarily realized by their particle

20   diameter ratio of 2.5. The char bed is occupying a position closer to the outlet, indicating it is

21   more likely to be entrained. This will effectively reduce the contact time between the char and the

22   generated product vapors, thus restricting further degradation of primary products. This also

23   implies that by gradual feeding of biomass just after the slots, the char will gradually be pushed

1 out instead of the biomass, while the completely converted biomass will be the source of "fresh"

2 char. This "self-cleaning" effect can be beneficial for several solid to gas/char processes.

3

## 6. Conclusions

5

6 The gas solid vortex reactor is a promising reactor technology for biomass fast pyrolysis. Cold

7 flow experiments with biomass-char mixtures demonstrate the ability of this reactor to selectively

8 retain biomass particles over long periods of time. The process intensification possibilities of the

9 vortex reactor technology are further demonstrated with various non-reactive and reactive, 3-D,

10 Euler-Euler CFD simulations of biomass fast pyrolysis. The numerical framework for these

11 simulations is validated with novel experimental data obtained on the setup where PIV recorded

12 solid azimuthal velocities show a reasonable match with the simulated data. Non-reactive

13 biomass-char simulations under a variety of loading ratios (1.5-4), feed temperatures (room

14 temperature vs pyrolysis temperature of 842 K) and diameter ratios (1-4) identify cut-off values

15 for which effective process intensification in terms of biphasic radial segregation is possible. The

16 radial separation of char and biomass observed in the GSVR is advantageous to achieve high

17 yields of bio-oil by reducing secondary degradation reactions by contact of product vapors with

18 char. Reactive simulations indicate that biomass particles need around 2 s to heat up to the

19 reaction temperature when fed to the reactor at room temperature and another 3 s to completely

20 convert to products if an average solids temperature of ~ 800 K is maintained in the reactor. High

21 convective heat transfer coefficients of 600 - 700 W m$^{-2}$ K$^{-1}$ illustrate the possibility of vortex

22 reactor technology to achieve isothermal biomass beds, essential for high bio-oil yields. The CFD

23 simulations show the process intensification via the effective segregation of biomass and char

24 particles during fast pyrolysis operation and the ability to produce bio-oil with yields up to 70 %.

1

## 7. Acknowledgements

1   Table 1 : Conservation Equations

---

**Mass Conservation**

$$\frac{\partial}{\partial t}\left(\alpha_q \rho_q\right) + \nabla \cdot \left(\alpha_q \rho_q \vec{v}_q\right) = \sum_{p=1}^{n}\left(\dot{m}_{pq} - \dot{m}_{qp}\right) + S_q$$

**Fluid Momentum Conservation**

$$\frac{\partial}{\partial t}\left(\alpha_q \rho_q \vec{v}_q\right) + \nabla \cdot \left(\alpha_q \rho_q \vec{v}_q \vec{v}_q\right) = -\alpha_q \nabla p + \nabla \cdot \bar{\bar{\tau}}_q + \alpha_q \rho_q \vec{g}$$

$$+ \sum_{p=1}^{n}\left(K_{pq}\left(\vec{v}_p - \vec{v}_q\right) + \dot{m}_{pq}\vec{v}_{pq} - \dot{m}_{qp}\vec{v}_{qp}\right)$$

$$+ \left(\vec{F}_{td,q}\right)$$

where $\bar{\bar{\tau}}_q$ is the stress-strain tensor of phase q:

$$\bar{\bar{\tau}}_q = \alpha_q \mu_q\left(\nabla\vec{v}_q + \nabla\vec{v}_q^T\right) + \alpha_q\left(\lambda_q - \frac{2}{3}\mu_q\right)\nabla \cdot \vec{v}_q\bar{I}$$

**Solid Momentum Conservation**

$$\frac{\partial}{\partial t}\left(\alpha_s \rho_s \vec{v}_s\right) + \nabla \cdot \left(\alpha_s \rho_s \vec{v}_s \vec{v}_s\right) = -\alpha_s \nabla p - \nabla p_s + \nabla \cdot \bar{\bar{\tau}}_s + \alpha_s \rho_s \vec{g}$$

$$+ \sum_{l=1}^{N}\left(K_{ls}(\vec{v}_l - \vec{v}_s) + \dot{m}_{ls}\vec{v}_{ls} - \dot{m}_{sl}\vec{v}_{sl}\right)$$

$$+ \left(\vec{F}_s + \vec{F}_{td,s}\right)$$

**Energy Conservation**

$$\frac{\partial}{\partial t}\left(\alpha_q \rho_q h_q\right) + \nabla \cdot \left(\alpha_q \rho_q \vec{u}_q h_q\right) = \alpha_q \frac{\partial p_q}{\partial t} + \bar{\bar{\tau}}_q : \nabla\vec{u}_q - \nabla\vec{q}_q + S_q$$

$$+ \sum_{p=1}^{N}\left(Q_{pq} + \dot{m}_{pq}h_{pq} - \dot{m}_{qp}h_{qp}\right)$$

**Transport equations for the turbulence kinetic energy, k and the specific dissipation rate, ω**

$$\frac{\partial}{\partial t}(\rho k) + \frac{\partial}{\partial x_i}(\rho k u_i) = \frac{\partial}{\partial x_j}\left(\Gamma_k \frac{\partial k}{\partial x_j}\right) + G_k - Y_k + S_k$$

$$\frac{\partial}{\partial t}(\rho \omega) + \frac{\partial}{\partial x_i}(\rho \omega u_i) = \frac{\partial}{\partial x_j}\left(\Gamma_\omega \frac{\partial \omega}{\partial x_j}\right) + G_\omega - Y_\omega + S_\omega$$

---

2

3

4

1    Table 2 : Constitutive equations

---

**Gas-Solid Drag Coefficient (Gidaspow)** [65]

$\beta = \frac{3}{4} C_D \frac{\epsilon_g \epsilon_s \rho_g |\overline{U_{slip}}|}{d_p} \epsilon_g^{-2.65}$ for $\epsilon_g > 0.8$

Where $C_D = 150 \frac{24}{\epsilon_g Re_s} \left[ 1 + 0.15 (\epsilon_g Re_s)^{0.687} \right]$ ; $Re = \frac{\rho_s d_p |\overline{U_{slip}}|}{\mu_g}$

$\beta = 150 \frac{\epsilon_s^2 \mu_g}{\epsilon_g d_p^2} + 1.75 \frac{\rho_g \epsilon_s |\overline{U_{slip}}|}{d_p}$ $\left( \text{for } \epsilon_g \leq 0.8 \right)$

**Solid-Solid Exchange Coefficient**

$K_{ls} = \dfrac{3(1 + e_{ls}) \left( \frac{\pi}{2} + C_{fr,ls} \frac{\pi^2}{8} \right) \alpha_s \rho_s \alpha_l \rho_l (d_l + d_s)^2 g_{0,ls}}{2\pi (\rho_l d_l^3 + \rho_s d_s^3)} |\vec{v}_l - \vec{v}_s|$

**Solids Pressure (Lun et al.)** [66]

$P_s = \alpha_s \rho_s \Theta_s + 2\rho_s (1 + e_{ss}) \alpha_s^2 g_{0,ss} \Theta_s$

**Radial Distribution Function (Ogawa et al.)** [66]

$g_{0,ll} = \left[ 1 - \left( \frac{\alpha_s}{\alpha_{s,max}} \right)^{\frac{1}{3}} \right]^{-1} + \frac{1}{2} d_l \sum_{k=1}^{N} \frac{\alpha_k}{d_k}$

where $\alpha_s = \sum_{k=1}^{N} \alpha_k$

**Solids Collisional Viscosity (Gidaspow et al.)** [65]

$\mu_{s,col} = \frac{4}{5} \alpha_s \rho_s d_s g_{0,ss} (1 + e_{ss}) \left( \frac{\Theta_s}{\pi} \right)^{\frac{1}{2}} \alpha_s$

**Solids Kinetic Viscosity (Syamlal, Rogers and O'brien )** [67]

$\mu_{s,kin} = \frac{\alpha_s d_s \rho_s \sqrt{\Theta_s \pi}}{6(3 - e_{ss})} \left[ 1 + \frac{2}{5} (1 + e_{ss})(3 e_{ss} - 1) \alpha_{ss} g_{0,ss} \right]$

**Solids Frictional Viscosity (Schaeffer)** [68]

$\mu_{s,fr} = \frac{p_s \sin \phi}{2 \sqrt{I_{2D}}}$

**Solids Bulk Viscosity (Lun et al.)** [69]

$\lambda_s = \frac{4}{3} \alpha_s^2 \rho_s d_s g_{0,ss} (1 + e_{ss}) \left( \frac{\Theta_s}{\pi} \right)^{\frac{1}{2}}$

**Shear Stress at the Wall (Johnson & Jackson)** [70]

$\vec{\tau}_s = -\frac{\pi}{6} \sqrt{3} \phi \frac{\alpha_s}{\alpha_{s.max}} \rho_s g_0 \sqrt{\Theta_s} \overrightarrow{U_{s,||}}$

**Granular Temperature (Lun et al.)** [54]

$\left( -P_s \overline{\overline{I}} + \overline{\overline{\tau}}_s \right) : \nabla \overline{U_S} - \gamma \Theta_S + 3\beta \Theta_S = 0$

---

2

1    Table 3 : Reaction network based on the work of Ranzi et al.[56] used for reactive fast pyrolysis

2    simulations in the vortex reactor.

3

| Reaction | | $A\ (s^{-1})$ | $E$ $(kJ\ mol^{-1})$ | $\Delta H$ $(kJ\ kg^{-1})$ |
|---|---|---|---|---|
| 1 | Cell → Cell A | $8 \cdot 10^{13}$ | 192.5 | 447.7 |
| 2 | Cell → 5 $H_2O$ + 6 Char | $8 \cdot 10^{7}$ | 125.5 | −1087.8 |
| 3 | Cell A → LVG | 4T | 41.8 | 732.2 |
| 4 | Cell A → 0.95 HAA + 0.25 Glyoxal + 0.2 Acetaldehyde + 0.25 HMFU + 0.2 Acetone +0.16 $CO_2$ + 0.23 CO + 0.9 $H_2O$ + 0.1 $CH_4$ + 0.61 Char | $1 \cdot 10^{9}$ | 133.9 | 899.6 |
| 5 | HCell → 0.4 HCell 1 + 0.6 HCell 2 | $1 \cdot 10^{10}$ | 129.7 | 548.1 |
| 6 | HCell 1 → 0.75 $H_2$ + 0.8 $CO_2$ + 1.4 CO + 0.5 Formaldehyde | $3 \cdot 10^{9}$ | 113.0 | 447.7 |
| 7 | HCell 1 → Xylan | 3T | 46.0 | 707.1 |
| 8 | HCell 2 → $CO_2$ + 0.5 $CH_4$ + 0.25 $C_2H_4$ + 0.8 CO + 0.8 $H_2$ + 0.7 Formaldehyde +0.25 Methanol + 0.125 Ethanol + 0.125 $H_2O$ + Char | $1 \cdot 10^{10}$ | 138.1 | 259.4 |
| 9 | LignC → 0.35 LignCC + 0.1 pCoumaryl + 0.08 Phenol + 0.41 $C_2H_4$ + $H_2O$ + 0.495 $CH_4$ +0.32 $CO_2$ + CO + $H_2$ + 5.735 Char | $4 \cdot 10^{15}$ | 202.9 | 602.5 |
| 10 | LignH → LignOH + Acetone | $2 \cdot 10^{13}$ | 156.9 | 523.0 |
| 11 | LignO → LignOH + $CO_2$ | $1 \cdot 10^{9}$ | 106.7 | 510.4 |
| 12 | LignCC → 0.3 pCoumaryl + 0.2 Phenol + 0.35 Acrylic-acid + 0.7$H_2O$ + 0.65 $CH_4$ +0.6 $C_2H_4$ + 1.8 CO + $H_2$ + 6.4 Char | $5 \cdot 10^{6}$ | 131.8 | 288.7 |
| 13 | LignOH → Lign + $H_2O$ + Methanol + 0.45 $CH_4$ + 0.2 $C_2H_4$ + 2 CO + 0.7 $H_2$ + 4.15 Char | $3 \cdot 10^{8}$ | 125.5 | 100.4 |
| 14 | Lign → Lumped-phenol | 8T | 50.2 | 577.4 |
| 15 | Lign → $H_2O$ + 2 CO + 0.2 Formaldehyde + 0.4 Methanol + 0.2 Acetaldehyde +0.2 Acetone + 0.6 $CH_4$ + 0.65 $C_2H_4$ + 0.5 $H_2$ + 5.5 Char | $1.2 \cdot 10^{9}$ | 125.5 | −209.2 |

4

5

1  Table 4 : Geometrical details and operating conditions used for Air-Aluminum CFD simulations

2  in the vortex reactor.

3

| Vortex geometrical details | |
|---|---|
| Reactor diameter | 80 mm |
| Reactor length | 15 mm |
| Exhaust diameter | 20 mm |
| Number of slots | 8 |
| Slot width | 1 mm |
| Operating conditions | |
| Primary Phase | Compressed Air |
| Inlet temperature | 289 K |
| Inlet Pressure | 110 kPa |
| Inlet flow rate | 45 Nm$^3$ h$^{-1}$ |
| Secondary Phase | Aluminum particles |
| Particle diameter | 0.5 mm |
| Particle density | 2700 kg m$^{-3}$ |
| Loading | 10.9 g |
| Specularity Coefficient | 0.05 |
| Restitution Coefficient | 0.85 |

4

5

6

1    Table 5 : Locations of pressure sensors in the reactor

2

| Location | Reactor Section | Radial Position | Axial Position |
|----------|-----------------|-----------------|----------------|
| 1 | Jacket | 55 mm | 0 mm |
| 2 | Bed | 38.5 mm | 15 mm |
| 3 | | 30.8 mm | 15 mm |
| 4 | Exhaust | 22.6 mm | 51.7 mm |
| 5 | | 20 mm | 47 mm |
| 6 | Top | 10 mm | 22.5 mm |
| 7 | Outlet | 55.3 mm | 71.6 mm |

3

4

1
2
3        1      Table 6 : Operating conditions and various inter-phase interactions implemented in the non-
4
5        2      reactive biomass-char and reactive biomass fast pyrolysis simulations.
6
7
8
9        3

| Biomass (Pine) | $\rho_b$ = 500 kg m$^{-3}$ |
|---|---|
| | $d_b$ = 0.5 mm |
| Char | $\rho_c$ = 450 kg m$^{-3}$ |
| | $d_c$ = 0.2 mm |
| Nitrogen inlet flow | 60 – 100 Nm$^3$ h$^{-1}$ |
| Nitrogen inlet temperature | 800 – 900 K |
| Solid feed | 5 – 10 g |
| Solid feed temperature | 298 K |
| Gas-Solid Drag | Gidaspow correlation[55] |
| Gas-Solid heat transfer | Gunn correlation[71] |
| Boundary conditions | Gas-wall : no-slip |
| | Biomass-wall : Specularity coefficient |
| | Char-wall : Specularity coefficient |
| Time step | 10$^{-4}$ s |
| Iterations per time step | 10 |
| Spatial accuracy | Second-order |
| Transient accuracy | First-order |
| Discretization Schemes | 2$^{nd}$ order upwind for pressure, momentum, density, temperature, turbulent kinetic energy. QUICK for volume fraction. |
| Pressure-Velocity Scheme | Coupled |

4

5

27
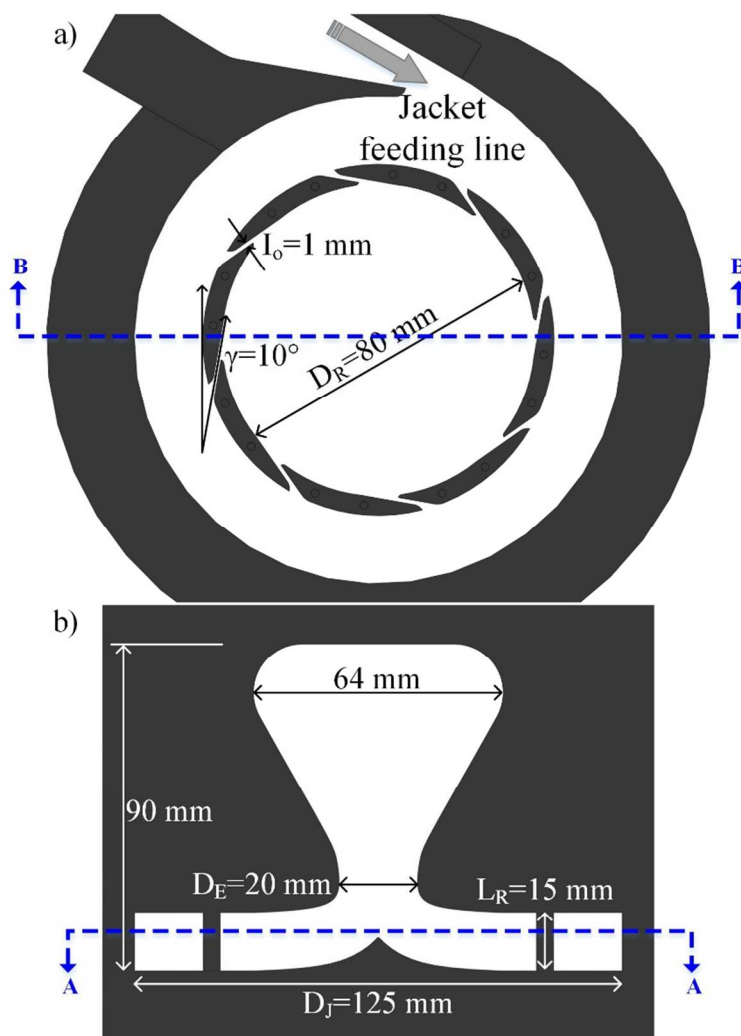
Fig. 1: Top and front views of the GSVR cross-section [Reprinted from Gonzalez-Quiroga et al[51] with permission from Elsevier]
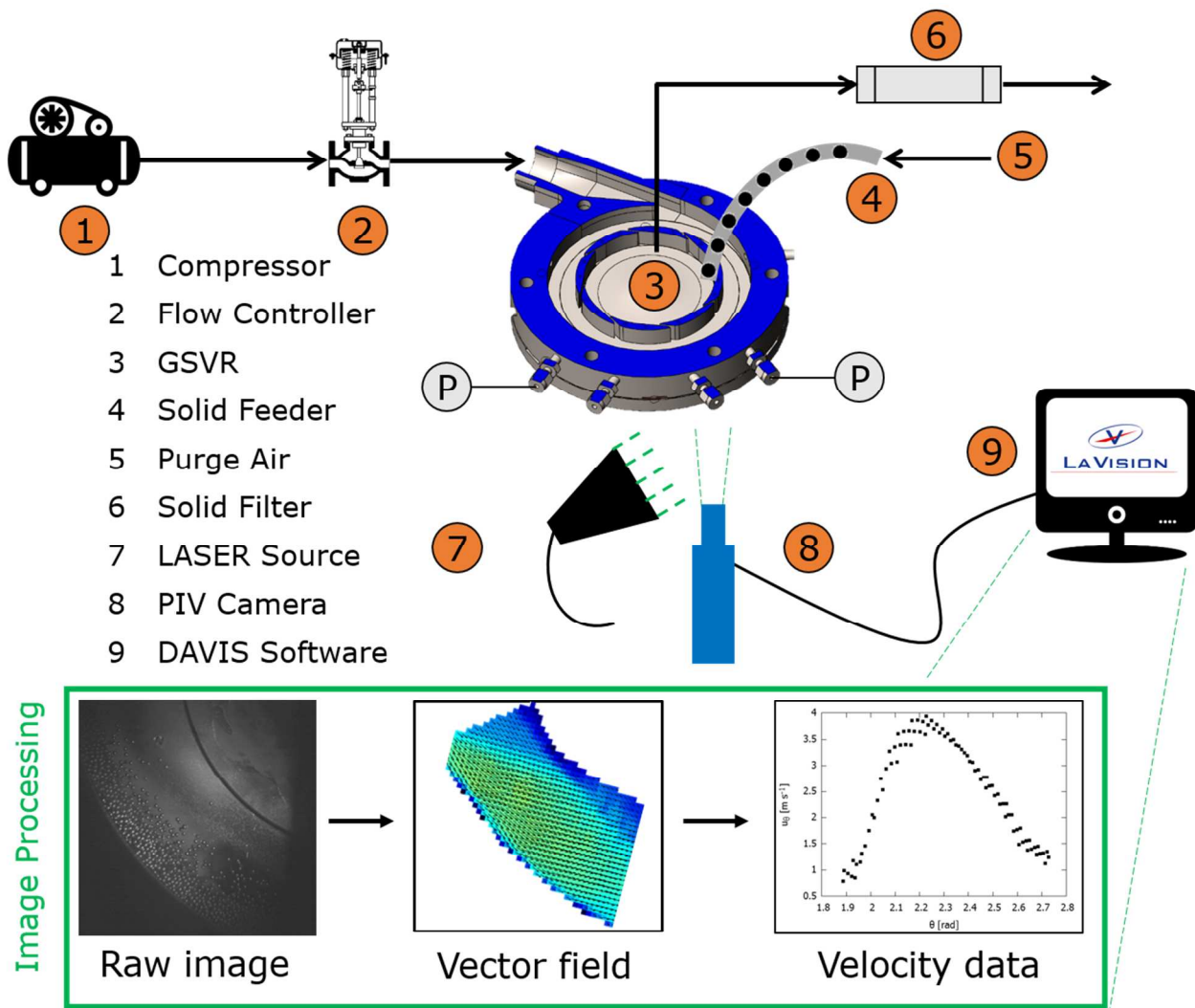
1
2
3          1
4
5
6
7
8
9
10
11
12
13
14          1    Compressor
15          2    Flow Controller
16          3    GSVR
17          4    Solid Feeder
18          5    Purge Air
19          6    Solid Filter
20          7    LASER Source
21          8    PIV Camera
22          9    DAVIS Software
23
24



Raw image          Vector field          Velocity data

28
29
30
31
32
33
34
35
36
37
38          2
39
40
41          3
42
43          4    Fig. 2 : Overview of the PIV setup and data processing procedure implemented.
44
45          5
46
47
48
49
50
51
52
53
54
55
56
57
58                                               29
59
60                              ACS Paragon Plus Environment

1
2
3      1
4
5
6
7
8
9
10
11
12
13
14
15
16
17
18
19
20
21
22
23
24     2
25
26     3
27
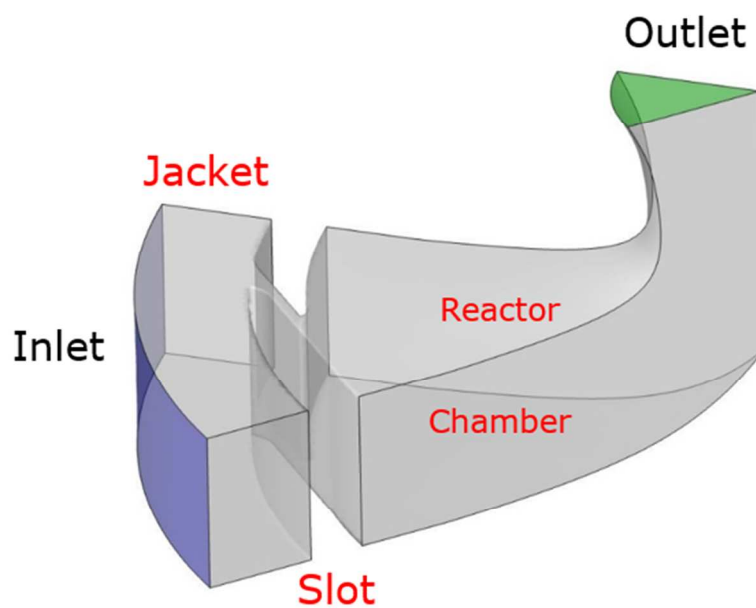28     4     Fig. 3 : 45$^{\circ}$ pie section of the vortex reactor used for CFD simulations.
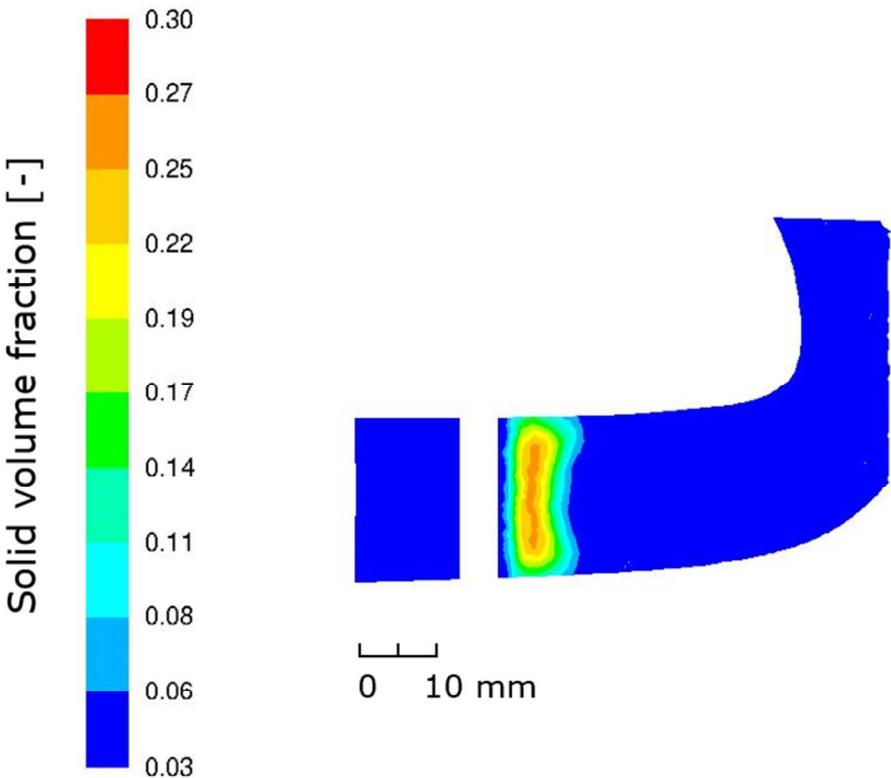
1

2

3        1



2

3

4    Fig. 4 : Angular plane midway of the simulated reactor pie section displaying Aluminum fraction

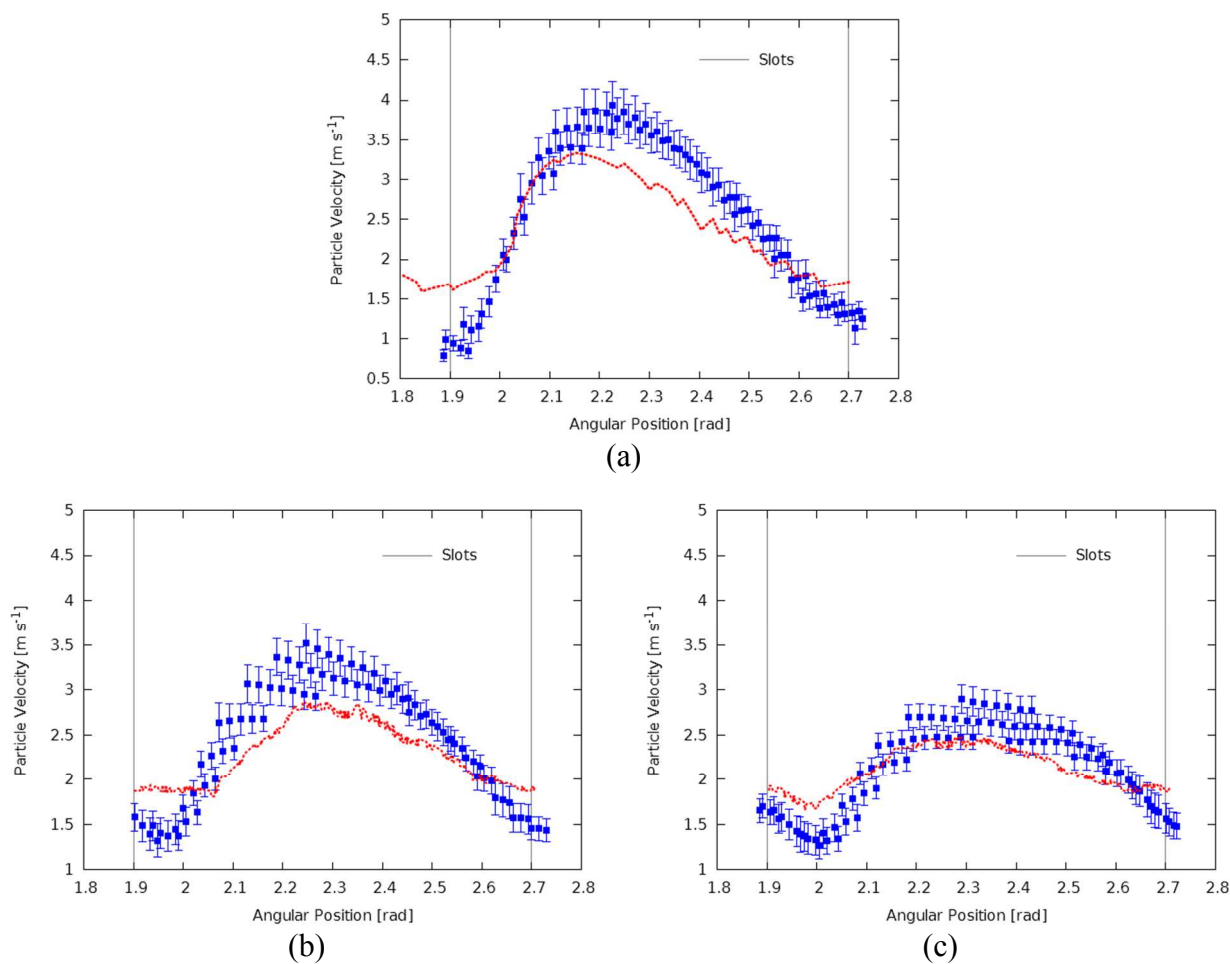5    of the bed. [Other simulation conditions in Table 4]

6

1



(a)



(b)



(c)

2

3 Fig. 5: Azimuthal particle velocities from PIV measurements (squares) and CFD simulations

4 (lines) at three radial positions: (a) r = 39 ± 0.5 mm ; (b) r = 38 mm ± 0.5 mm ; & (b) r = 37 mm

5 ± 0.5 mm. [Other simulations conditions in Table 4]

6

1
2
3          1
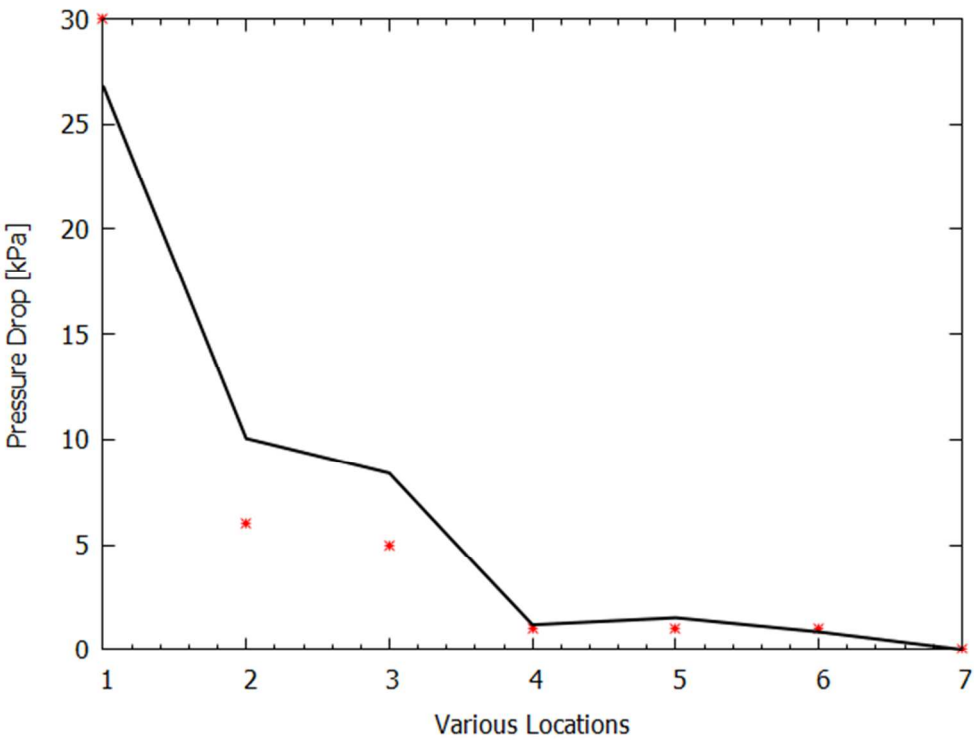4
5          2
6
7



3
4

5    Fig. 6 Experimental [points] and CFD simulated [line] pressures (with respect to the outlet

6    pressure) at various locations in the reactor for Air-Aluminium system. [Other simulation

7    conditions in Table 4. Locations of various sensors identified in Table 5.]

8
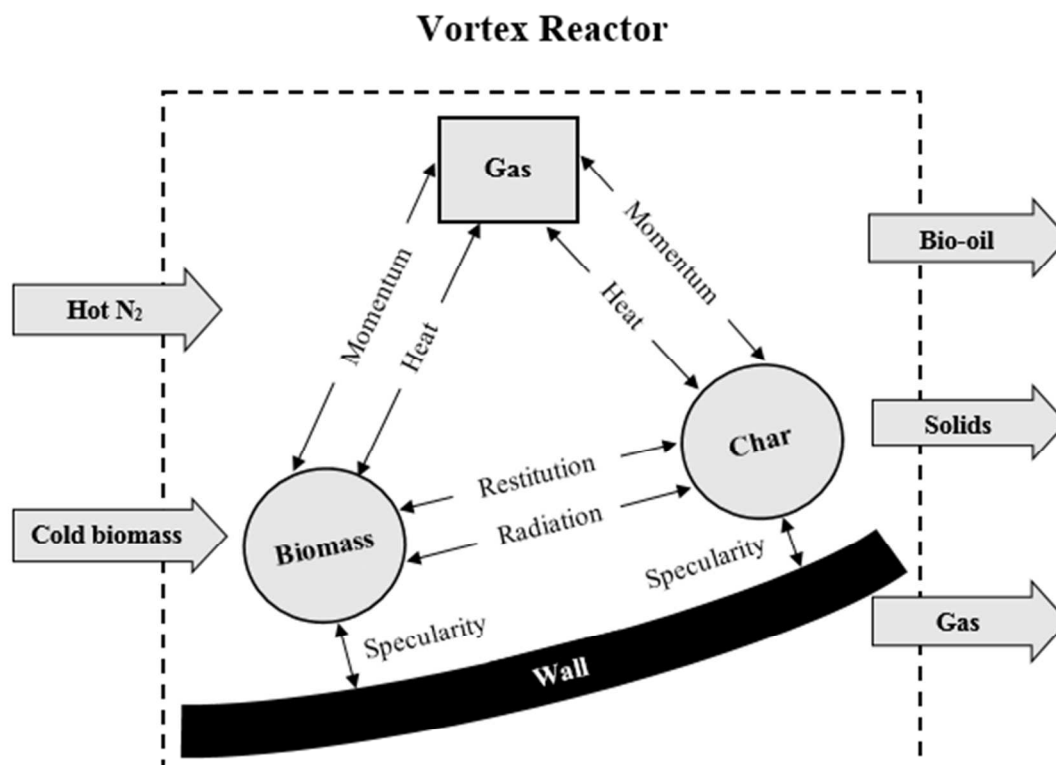
1

**Vortex Reactor**



2

3

4  Fig. 7 : Schematic representation of various inter-phase and phase-wall transport interactions in

5  the vortex reactor as considered in the simulations. [refer to Table 2 and Table 6 for more details]
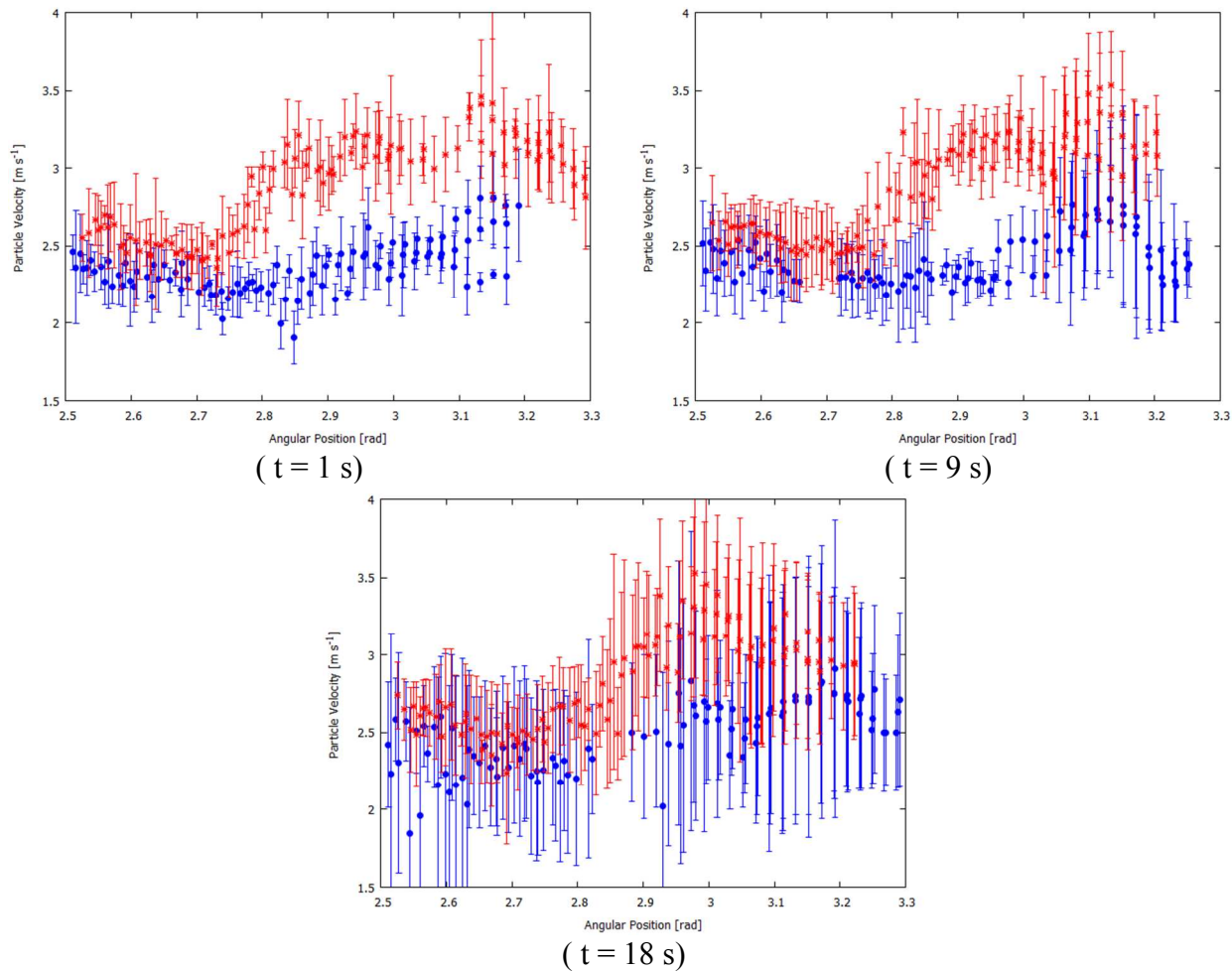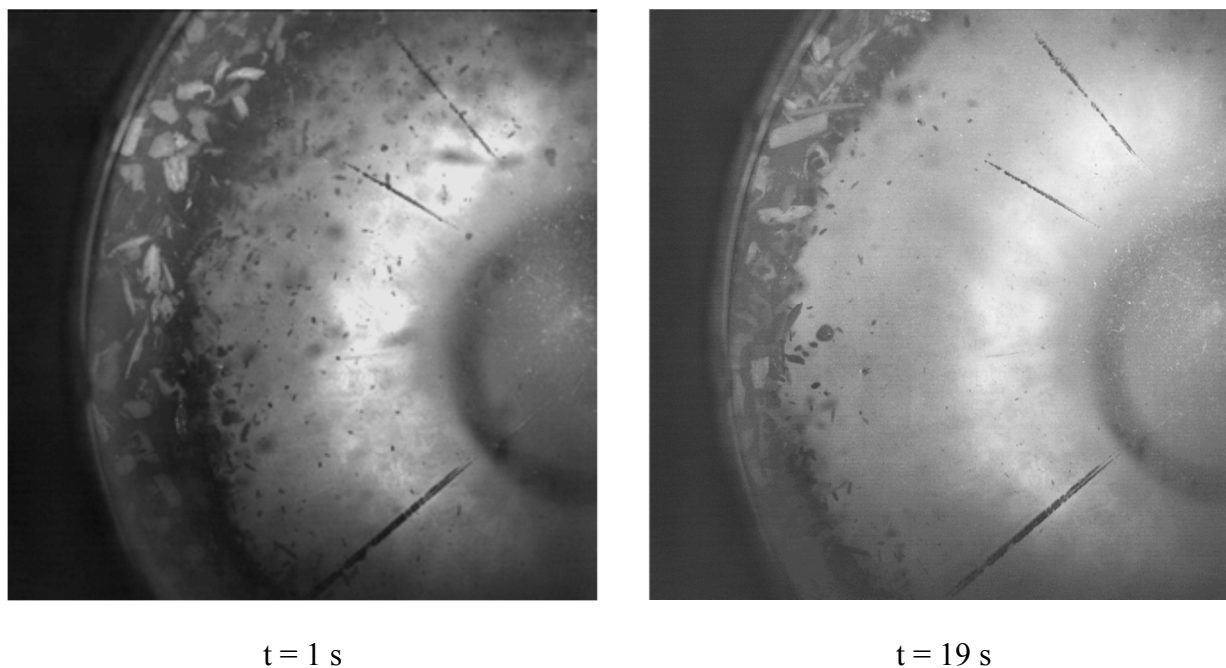
6

1

2



( t = 1 s) ( t = 9 s)



( t = 18 s)

3

4   Fig. 8 : Variation of bed azimuthal velocities    at two radial positions for three time

5   measurements. (red : r = 38 ± 0.5 mm , blue : r = 34 ± 0.5 mm)

6

t = 1 s                                    t = 19 s

1

2    Fig. 9 : Temporal evolution of biomass-char bed highlighting selective entrainment of the char

3    particles. Fine char particles present in the freeboard of the reactor (small black particles) are

4    carried away with air and a relative clean freeboard region without char is seen in the second
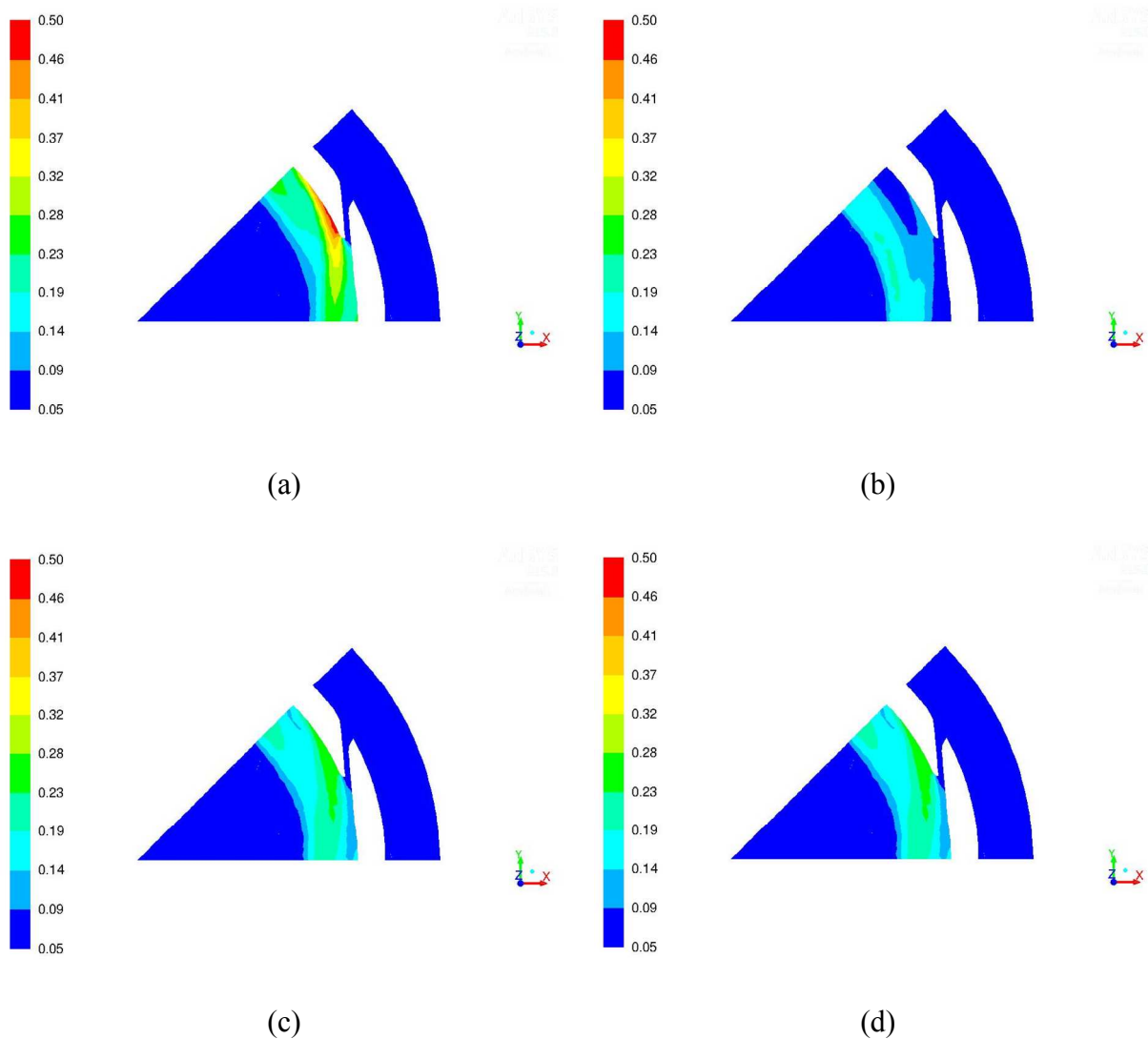
5    image.

6

(a)                                                              (b)

(c)                                                              (d)

1

2  Fig. 10 : Effect of biomass to char diameter ratio ($d_r$) on segregation in the reactor. (a) biomass

3  v.f. for biomass-char diameter ratio of 2.5 ; (b) char v.f. for biomass-char diameter ratio of 2.5 ;

4  (c) biomass v.f. for biomass-char diameter ratio of 1 ; (d) char v.f. for biomass-char diameter

5  ratio of 1. All fields are displayed on z = 10 mm axial plane. [Other simulation conditions in
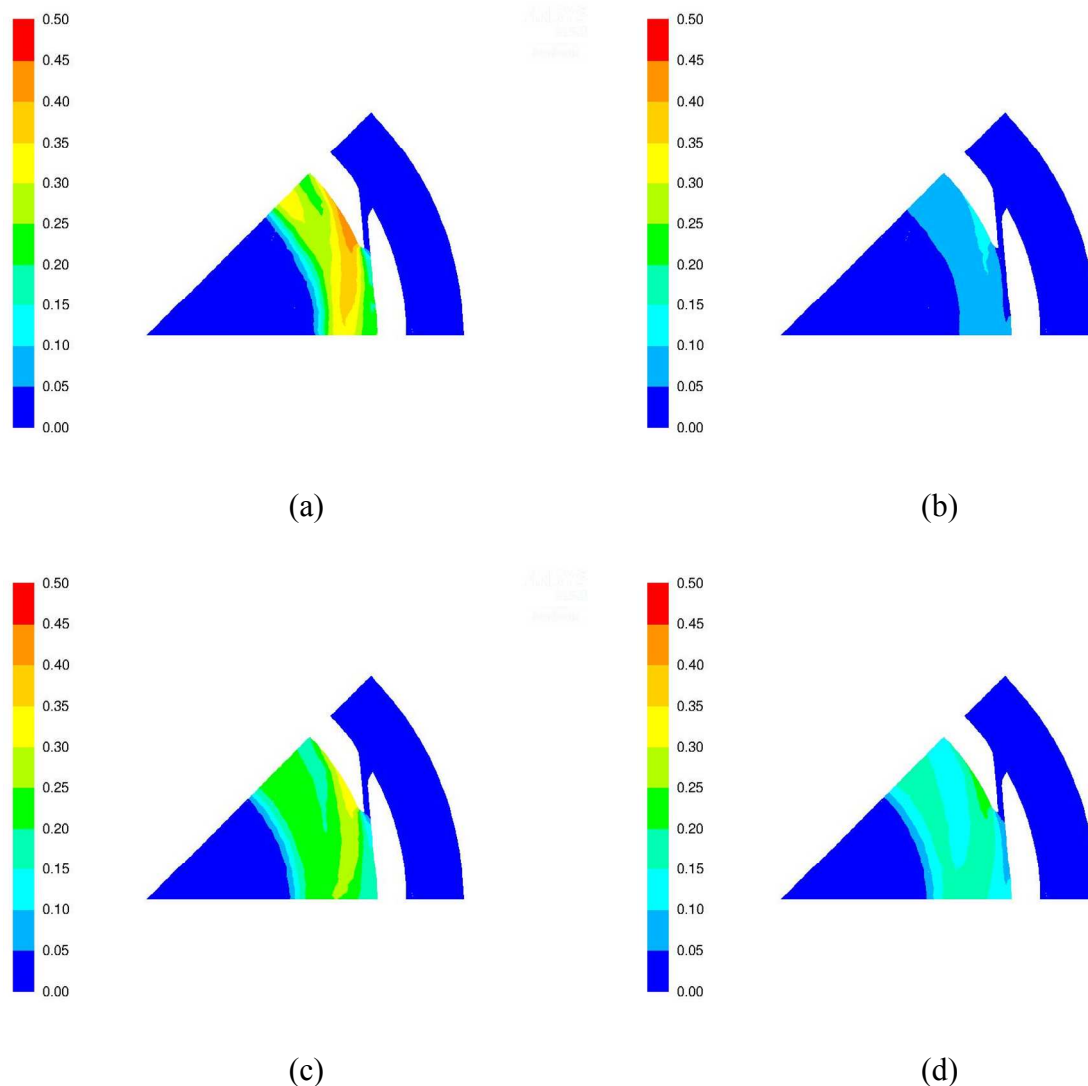
6  Table 6.]

7

1

2    Fig. 11 : Effect of biomass to char loading ratio on segregation in the reactor: (a) biomass v.f. for

3    loading ratio 1.5; (b) char v.f. for loading ratio 1.5; (c) biomass v.f. for loading ratio 4 and (d)

4    char v.f. for loading ratio 4. All fields are displayed on z = 10 mm axial plane. [Other simulation
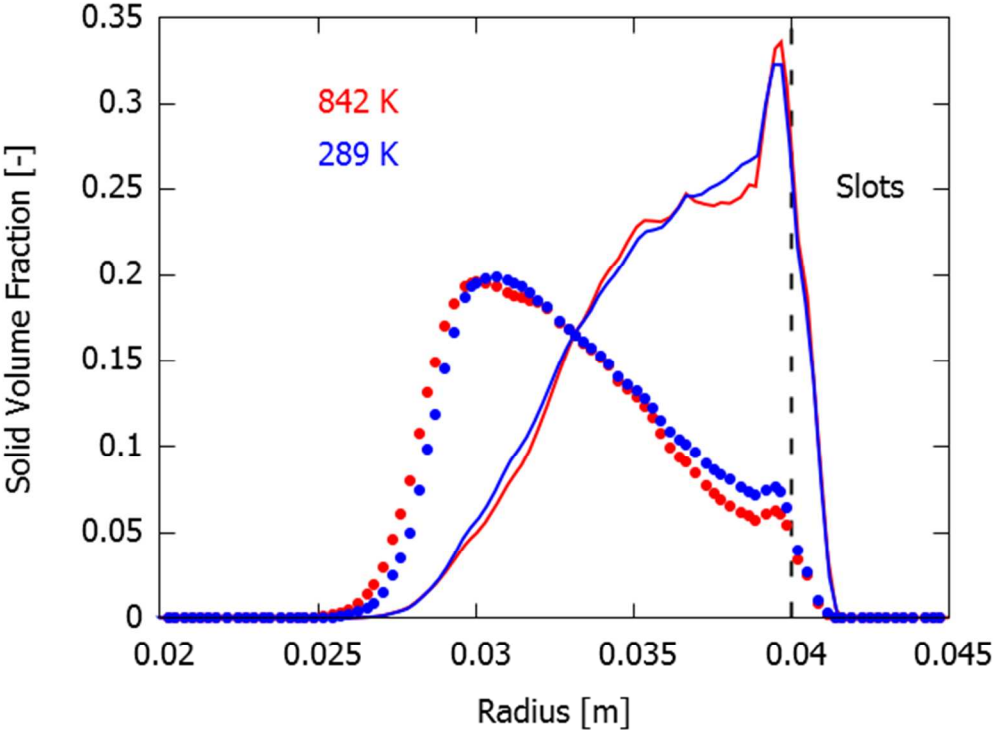
5    conditions in Table 6]

6

Fig. 12 : Effect of operating temperature on segregation in the reactor for a 60-40 % biomass-char

mixture being fed to the vortex reactor under cold (289 K) and hot (842 K) operating conditions.

Solid lines: biomass; dots: char. All fields are displayed on z = 10 mm axial plane. [Other

simulation conditions in Table 6]

(a)                                                          (b)

1

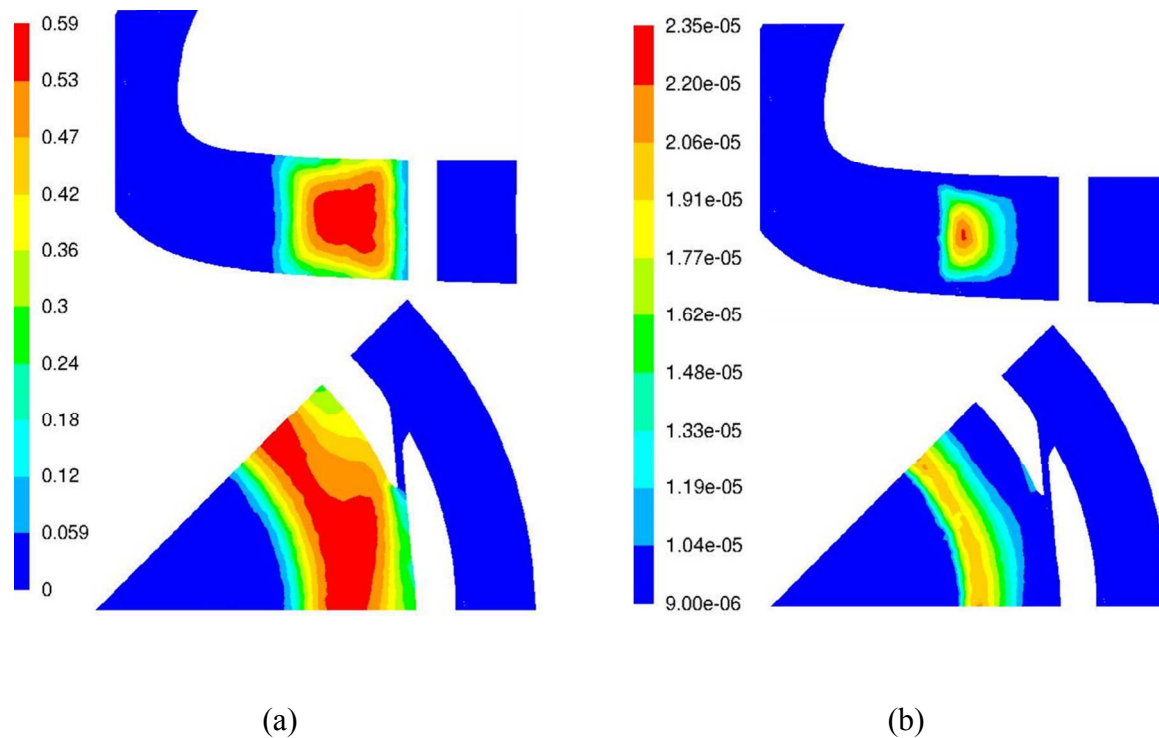2    Fig. 13 : Solid volume fractions for (a) biomass and (b) char for the base case of gas inlet flow of

3    60 Nm$^3$ h$^{-1}$ and gas inlet temperature of 842 K. Top: midway azimuthal plane, bottom: z = 10 mm

4    axial plane. [Other simulation conditions in Table 6]

5

1

2

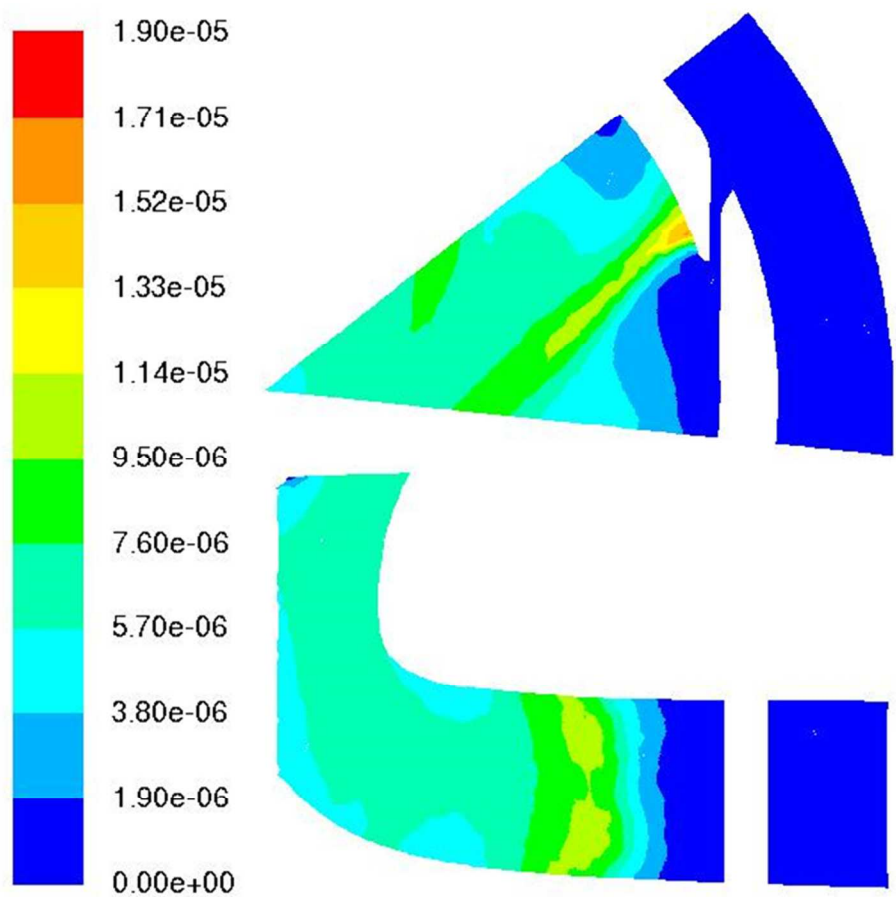3    Fig. 14 : Instantaneous mass fraction fields of phenol as observed during reactive simulations of

4    the base case of gas inlet flow of 60 Nm$^3$ h$^{-1}$ and gas inlet temperature of 842 K. Top: z = 10 mm

5    axial plane; bottom: midway azimuthal plane. flow time = 1.7 s, [Other simulation conditions in
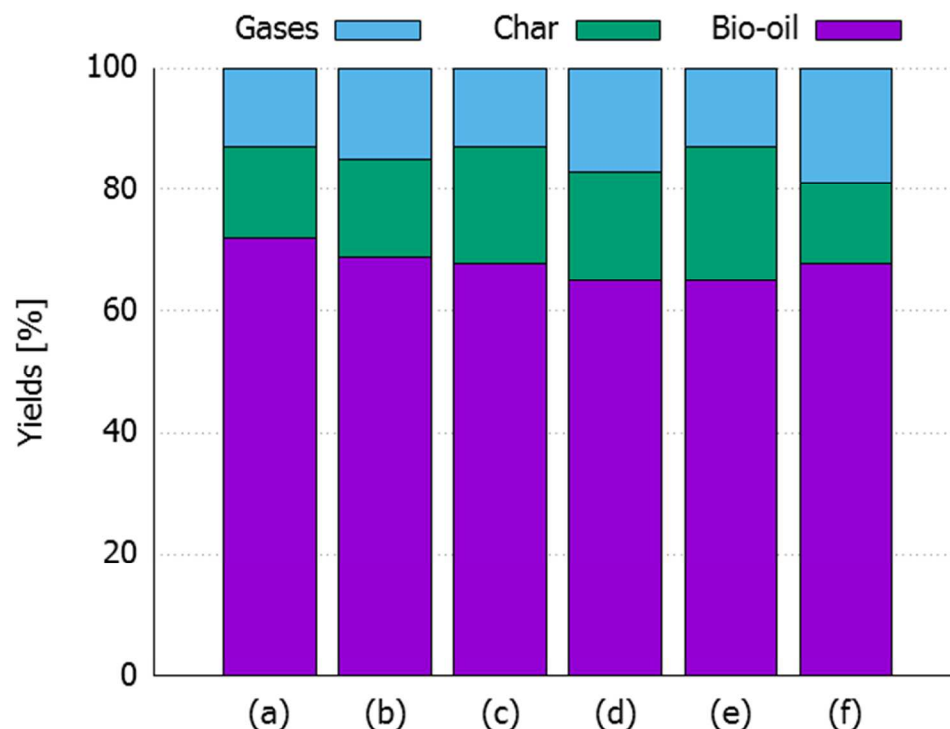
6    Table 6]

7

1



2

3    Fig. 15 : Simulated yields of gas, char and bio-oil as function of process conditions. (a) nitrogen

4    inlet flow rate of 70 Nm$^3$ h$^{-1}$ and inlet temperature of 842 K; (b) nitrogen inlet flow rate of 100

5    Nm$^3$ h$^{-1}$ and inlet temperature of 842 K; (c) nitrogen inlet flow rate of 70 Nm$^3$ h$^{-1}$ and inlet

6    temperature of 800 K; (d) nitrogen inlet flow rate of 60 Nm$^3$ h$^{-1}$ and inlet temperature of 900 K;

7    (e) nitrogen inlet flow rate of 40 Nm$^3$ h$^{-1}$ and inlet temperature of 842 K; (f) nitrogen inlet flow

8    rate of 50 Nm$^3$ h$^{-1}$ and inlet temperature of 842 K; [Other simulation conditions in Table 6]

9
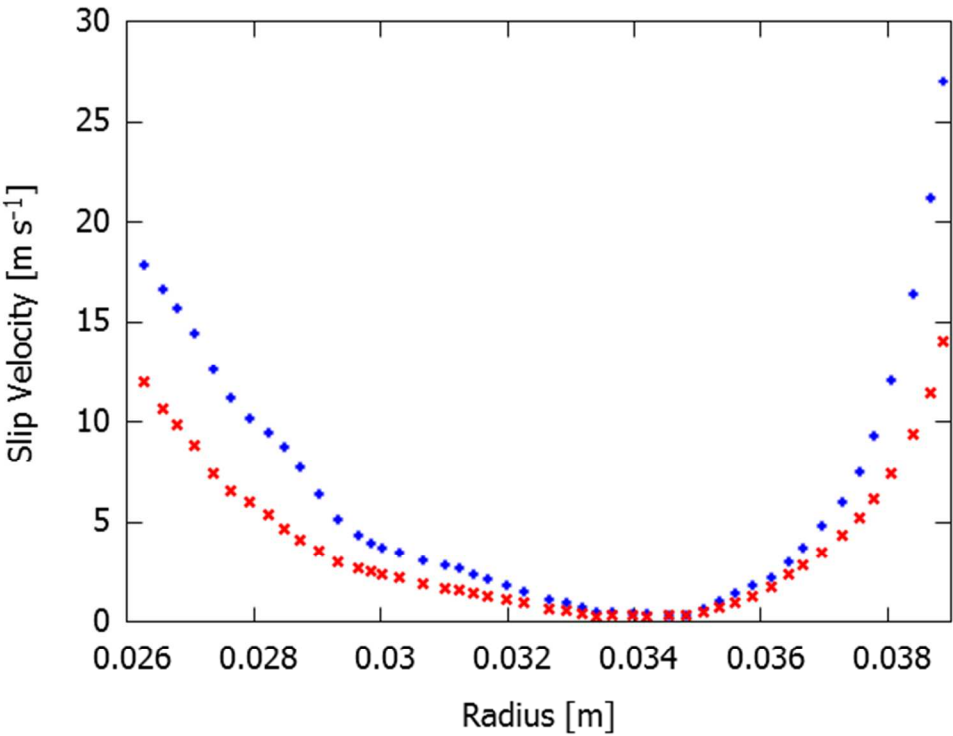
Fig. 16 : Circumferentially averaged slip velocity magnitude versus radius across the biomass bed for 60 (x) and 100 (+) $Nm^3$ $h^{-1}$. Velocities are calculated on z = 10 mm axial plane. [Other simulation conditions in Table 6].
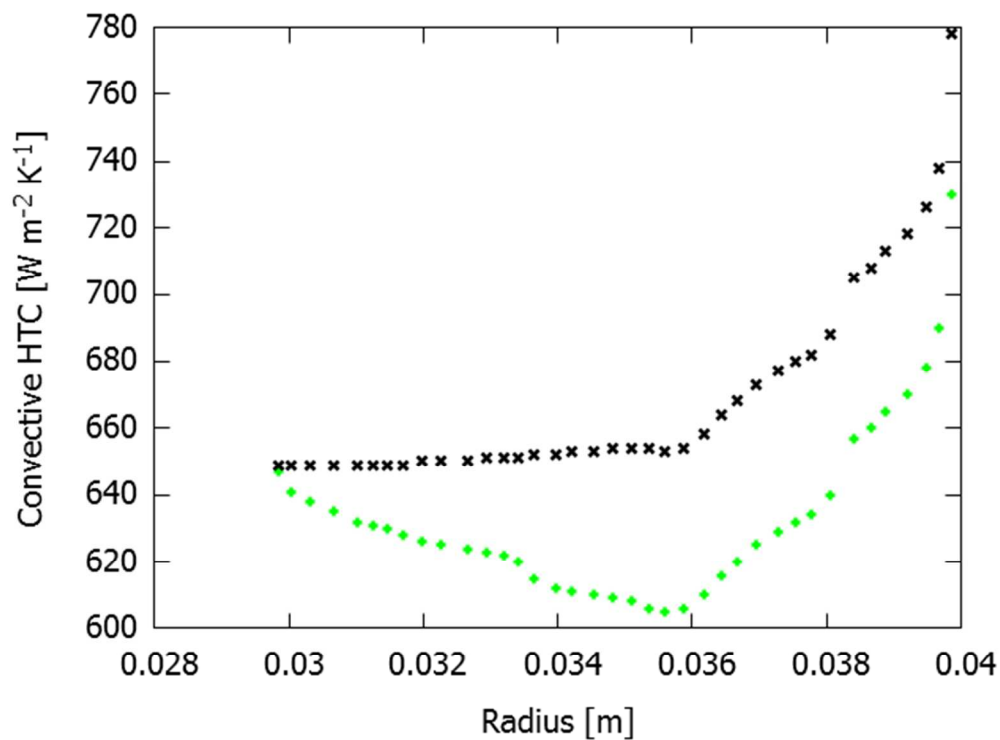
Fig. 17 : Convective gas-solid heat transfer coefficient versus radius across the biomass bed for

60 (+) and 100 (x) $Nm^3 h^{-1}$. Velocities are calculated on z = 10 mm axial plane[Other simulation

conditions in Table 6].

1
2
3    1    **Supporting information**
4

5
6    2
7

8    3    Table S 1 : Physical properties of the biomass constituents used during reactive fast pyrolysis
9

10
11   4    simulations
12

13
14   5

| Component | MW (g mol$^{-1}$) | $\rho$ (kg m$^{-3}$) | Cp (J kg$^{-1}$ K$^{-1}$) | $\lambda$ (W m$^{-1}$ K$^{-1}$) |
|---|---|---|---|---|
| Cell | 162 | 500 | 1400 | 0.209 |
| Cell A | 162 | 500 | 1400 | 0.209 |
| HCell | 100 | 500 | 1400 | 0.209 |
| HCell 1 | 100 | 500 | 1400 | 0.209 |
| HCell 2 | 100 | 500 | 1400 | 0.209 |
| LignC | 258.27 | 500 | 1400 | 0.209 |
| LignH | 422.38 | 500 | 1400 | 0.209 |
| LignO | 436.45 | 500 | 1400 | 0.209 |
| LignOH | 378.37 | 500 | 1400 | 0.209 |
| LignCC | 373.87 | 500 | 1400 | 0.209 |
| Lign | 208.21 | 500 | 1400 | 0.209 |

44   6
45
46
47   7
48
49
50
51
52
53
54
55
56
57
58                                    45
59

## S-1 Reactive UDF Validation

In order to validate the reactive UDF used for GSVR simulations, it was implemented for a Drop Tube Reactor (DTR) from literature [57]. A DTR is beneficial for studying pyrolysis kinetics under purely kinetic regime, by providing high and isothermal temperatures, due to a high heat flux. Due to these virtues, DTRs usually demonstrate high yields of bio-oil from them. Biomass fast pyrolysis simulations were performed on a 2D geometry of the reactor with simulation domain reduced to a plane of 0.075 m width and 1.2 m length. The structured mesh in this domain consisted of ~ 5,000 cells. Hot Nitrogen and biomass are fed at the top of the reactor. Side walls are heated to temperatures between 723 – 823 K as required in order to impose near isothermal conditions inside the reactor. Products exit from the outlet located at the bottom end of the reactor. Simulations are performed within an Eulerian framework using the kinetic model proposed by Ranzi et al., 2008 [56] that is shown in Table 3 of the manuscript. For ease of handling, simulation is performed within a 3-phase framework. Gas phase is formed of nitrogen and pyrolysis products. Virgin and activated biomass components form the first solid phase while char is modeled as another solid phase. Simulations are performed with a time step of $10^{-2}$ s for most of the flow time, except for at the start of the simulations, during biomass feeding, a time-step of $10^{-3}$ s is adopted. During these simulations, second order spatial accuracy and first order temporal accuracy is used. Finally, the reaction kinetics UDF used in GSVR simulations is also used in these simulations in order to compare simulation results with the experimental data and to further validate the UDF.

1    Predicted and measured yields of key pyrolysis products: phenol, formaldehyde and levoglucosan

2    are compared further. The comparisons are made for the set of operating conditions from the

3    original article, enlisted further in Table S 2.

4

5    Table S 2 : Simulation conditions for DTR simulations

| Run No | Run ID | Biomass dp (µm) | Temperature (°C) | Gas residence time (s) |
|--------|--------|-----------------|------------------|------------------------|
| 1 | Run-450 °C | 370 | 450 | 16.6 |
| 2 | Run-500 °C | 370 | 500 | 16.6 |
| 3 | Run-550 °C | 370 | 550 | 16.6 |
| 4 | Run-600 °C | 370 | 600 | 16.6 |
| 5 | Run-490 µm | 490 | 550 | 16.6 |
| 6 | Run-640 µm | 640 | 550 | 16.6 |

6



(a)                                                                                            (b)

(c)

1
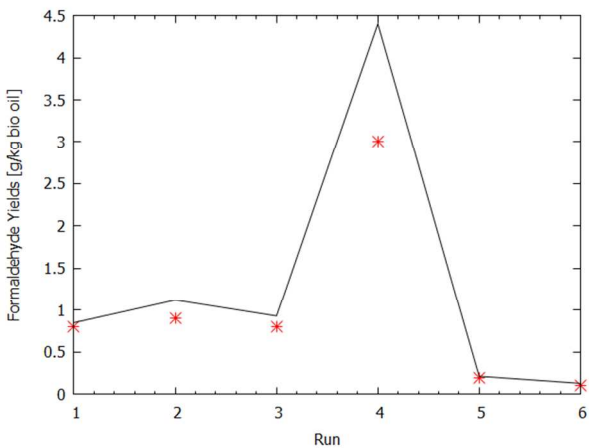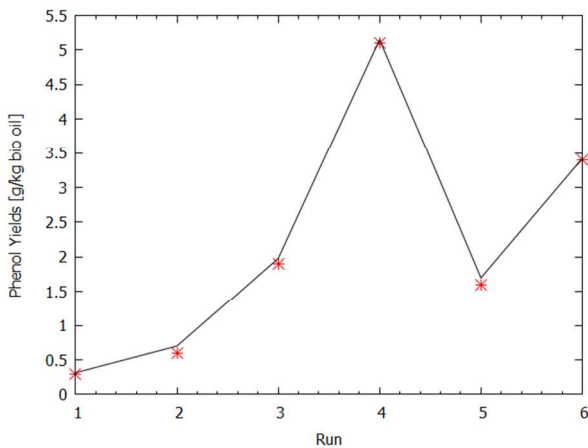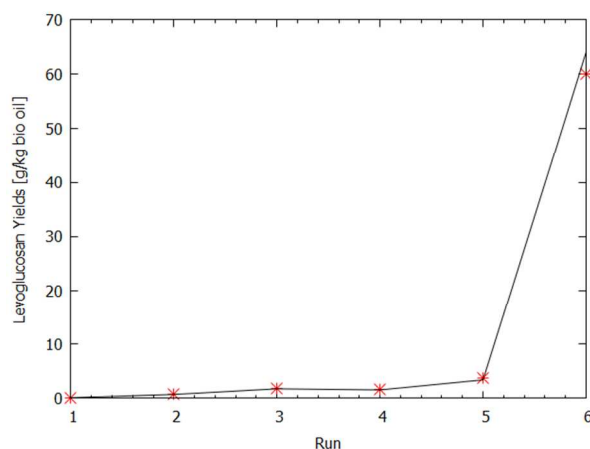
2   Fig. S 1 : Comparison between experimental [points] and CFD simulated [lines] yields for (a)

3   Formaldehyde, (b) Phenol & (c) Levoglucosan for various runs for a Drop Tube Reactor (DTR).

4   Run details enlisted in Table S 2.

5

6   As seen from Fig. S 1, the overall CFD simulated results well represent the global trends in the

7   production for the three pyrolysis products studied. In case of formaldehyde (Fig. S 1 (a)),

8   simulations consistently predict higher yields as compared to the experimental data. This could

9   be attributable to presence of secondary degradation of formaldehyde inside the reactor before

10  exiting, as the CFD model does not account for secondary pyrolysis reactions. Thus, it is likely

11  that the relatively lower experimental yields observed by the authors as compared to the CFD

12  simulations is a result of ancillary reactions. Run 4 shows the highest discrepancy owing to high

13  formaldehyde yields pertaining, which would thus show higher tendency to reduce to side

14  products upon degradation.

15

1   On the other hand, the predicted and recorded phenol yields agree well (Fig. S 1 (b)). The trends

2   of rising phenol yields with temperature, as well as with increasing particle diameter are in

3   agreement with the experiments. Phenol as a molecule doesn't show considerable thermal

4   degradation for temperatures < 1375 K [72]. Thus, the formed phenol fractions from biomass will

5   not be prone to secondary degradation and further reduction in yield thereof. As the CFD kinetic

6   model is also based solely on primary pyrolysis reactions, the agreement between experiments

7   and simulations can be justified.

8

9   Lastly, the levoglucosan yields from simulations are able to capture the increasing yields with

10   various runs (Fig. S 1 (c)). For Run 6 however, although the trend in levoglucosan yields is

11   predicted by the CFD model, the simulated values are higher than the ones experimentally

12   reported. For the 640 µm particles pyrolyzed during this run, the biomass particle doesn't react

13   completely before exiting the reactor. Thermally thick biomass particles typically result in high

14   levoglucosan yields, as levoglucosan is one of the initial products during cellulose pyrolysis [73][74].

15   This postulation is in accordance with the experimental observations by Guizani et al [57]; which

16   are further conforming to the simulated predictions.

17

18   Lastly, overall yields of liquids (bio-oil) and solids (char) from experiments are compared with

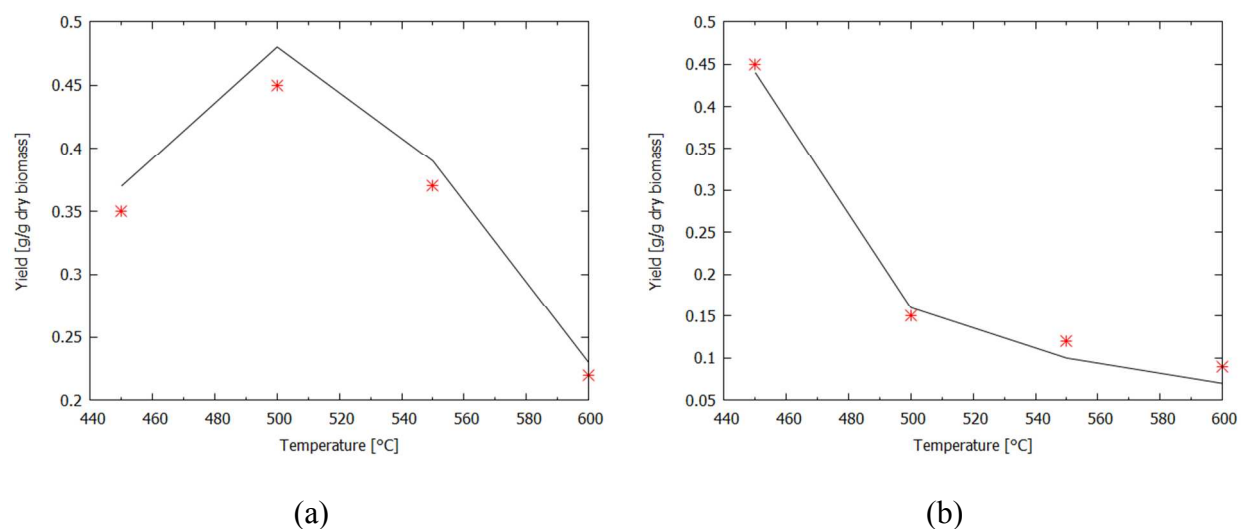19   the CFD simulations, as a function of reactor temperature.

20

(a)                                                             (b)

1

2    Fig. S 2 : Comparison of experimental [points] and simulated [lines] yields for (a) bio-oil and (b)

3    char.

4

5    Fig. S 2 (a) & (b) shows that although some discrepancies exist, the CFD model correctly

6    represents the experimental yields and their dependencies on the reactor temperature. The bio-oil

7    yields are highest at 500 °C operation temperature, conforming to the observations made in the

8    literature [5]. On the other hand, char yields decrease with increase in temperature as the heat influx

9    to biomass particles is faster at higher temperatures, increasing the conversion of lignocellulosic

10   biomass to condensable bio-oil fraction.

11

12   The overall product yields and the individual component yields comparisons between the

13   experiments and CFD simulations show a good agreement. The trends observed experimentally

14   are also captured by the simulations. Thus, it can be claimed that the reactive UDF used for

15   simulating a DTR and eventually to simulate the GSVR is validated.

16

Nomenclature

| | |
|---|---|
| $C_p$ | Heat capacity (J kg$^{-1}$ K$^{-1}$) |
| $d_b$ | Biomass particle diameter (m) |
| $d_c$ | Char particle diameter (m) |
| $\rho_b$ | Biomass density (kg m$^{-3}$) |
| $\rho_c$ | Char density (kg m$^{-3}$) |
| $u_{slip}^{az}$ | Azimuthal slip velocity (m s$^{-1}$) |
| $d_r$ | Biomass to char diameter ratio (-) |
| $\rho_r$ | Biomass to char density ratio (-) |
| $\varepsilon_g$ | Gas volume fraction or Voidage (-) |
| $\varepsilon_s$ | Solid volume fraction: 1- $\varepsilon_g$ (-) |
| $h$ | Convective heat transfer coefficient (W m$^{-2}$ K$^{-1}$) |
| $r$ | Radial position (m) |
| $z$ | Axial position (m) |
| $I_0$ | Slot width (m) |
| $N_s$ | Number of slots (-) |
| $L_R$ | Length of the vortex reactor (m) |
| $L_E$ | Total length of the vortex reactor including the exhaust section (m) |
| $\gamma$ | Angle of slot opening w.r.t. the tangent ($^{\circ}$) |
| $\Delta P_{bed}$ | Pressure drop over the solid bed (kPa) |
| $\Delta P_{total}$ | Pressure drop over the vortex reactor (kPa) |
| $D_R$ | Reactor diameter (m) |
| $D_E$ | Exhaust diameter (m) |

$D_J$        Jacket diameter (m)

$E$        Activation Energy for reaction (kJ mol$^{-1}$)

$\Delta H$        Heat of reaction (kJ kg$^{-1}$)

$A_f$        Pre-exponential factor (s$^{-1}$)

$e_{ss}$        Restitution coefficient

$\varphi$        Specularity coefficient

$g$        Acceleration due to gravity (m s$^{-2}$)

$\theta_s$        Granular temperature (m$^2$ s$^{-2}$)

$\vec{F}_{td,q}$        Turbulent dispersion force

Abbreviations

Cell        Cellulose

HCell        Hemicellulose

LignC/H/O        Lignin C; Lignin H; Lignin O

KTGF        Kinetic Theory of Granular Flow

CFD        Computational Fluid Dynamics

GSVR        Gas Solid Vortex Reactor

Freeboard        Region between solid bed edge and exhaust containing isolated solid particles flowing in a non-uniform pattern

1

52

**References**

1. Dincer, I., Renewable energy and sustainable development: a crucial review. *Renewable and sustainable energy reviews* **2000,** 4, (2), 157-175.

2. World Energy Perspective: Cost of Energy Technologies. https://www.worldenergy.org/wp-content/uploads/2013/09/WEC_J1143_CostofTECHNOLOGIES_021013_WEB_Final.pdf

3. Mettler, M. S.; Vlachos, D. G.; Dauenhauer, P. J., Top ten fundamental challenges of biomass pyrolysis for biofuels. *Energy & Environmental Science* **2012,** 5, (7), 7797-7809.

4. Sanderson, K., US biofuels: A field in ferment. In Nature Publishing Group: 2006.

5. Bridgwater, A. V., Review of fast pyrolysis of biomass and product upgrading. *Biomass and Bioenergy* **2012,** 38, 68-94.

6. Djokic, M. R.; Dijkmans, T.; Yildiz, G.; Prins, W.; Van Geem, K. M., Quantitative analysis of crude and stabilized bio-oils by comprehensive two-dimensional gas-chromatography. *Journal of Chromatography A* **2012,** 1257, 131-140.

7. Zhang, Q.; Chang, J.; Wang, T.; Xu, Y., Review of biomass pyrolysis oil properties and upgrading research. *Energy conversion and management* **2007,** 48, (1), 87-92.

8. Gonzalez-Quiroga, A.; Van Geem, K. M.; Marin, G. B., Towards first-principles based kinetic modeling of biomass fast pyrolysis. *Biomass Conversion and Biorefinery* **2017,** 7, (3), 305-317.

9. Robinson, J.; Dodds, C.; Stavrinides, A.; Kingman, S.; Katrib, J.; Wu, Z.; Medrano, J.; Overend, R., Microwave Pyrolysis of Biomass: Control of Process Parameters for High Pyrolysis Oil Yields and Enhanced Oil Quality. *Energy & Fuels* **2015,** 29, (3), 1701-1709.

1    10.    Huber, G. W.; Corma, A., Synergies between bio and oil refineries for the production of

2    fuels from biomass. *Angewandte Chemie International Edition* **2007,** 46, (38), 7184-7201.

3    11.    Mohan, D.; Pittman, C. U.; Steele, P. H., Pyrolysis of wood/biomass for bio-oil: a critical

4    review. *Energy & fuels* **2006,** 20, (3), 848-889.

5    12.    Anca-Couce, A., Reaction mechanisms and multi-scale modelling of lignocellulosic

6    biomass pyrolysis. *Progress in Energy and Combustion Science* **2016,** 53, 41-79.

7    13.    Aramideh, S.; Xiong, Q.; Kong, S.-C.; Brown, R. C., Numerical simulation of biomass

8    fast pyrolysis in an auger reactor. *Fuel* **2015,** 156, 234-242.

9    14.    Trendewicz, A.; Braun, R.; Dutta, A.; Ziegler, J., One dimensional steady-state circulating

10    fluidized-bed reactor model for biomass fast pyrolysis. *Fuel* **2014,** 133, 253-262.

11    15.    Xue, Q.; Heindel, T.; Fox, R., A CFD model for biomass fast pyrolysis in fluidized-bed

12    reactors. *Chemical Engineering Science* **2011,** 66, (11), 2440-2452.

13    16.    Papadikis, K.; Gu, S.; Bridgwater, A. V.; Gerhauser, H., Application of CFD to model

14    fast pyrolysis of biomass. *Fuel Processing Technology* **2009,** 90, (4), 504-512.

15    17.    Ranganathan, P.; Gu, S., Computational fluid dynamics modelling of biomass fast

16    pyrolysis in fluidised bed reactors, focusing different kinetic schemes. *Bioresource technology*

17    **2016**.

18    18.    Wang, S.; Lu, H.; Zhao, F.; Liu, G., CFD studies of dual circulating fluidized bed reactors

19    for chemical looping combustion processes. *Chemical Engineering Journal* **2014,** 236, 121-130.

20    19.    Zimmermann, S.; Taghipour, F., CFD modeling of the hydrodynamics and reaction

21    kinetics of FCC fluidized-bed reactors. *Industrial & engineering chemistry research* **2005,** 44,

22    (26), 9818-9827.

1    20.    Klimanek, A.; Adamczyk, W.; Katelbach-Woźniak, A.; Węcel, G.; Szlęk, A., Towards a

2    hybrid Eulerian–Lagrangian CFD modeling of coal gasification in a circulating fluidized bed

3    reactor. *Fuel* **2015,** 152, 131-137.

4    21.    Papadikis, K.; Bridgwater, A.; Gu, S., CFD modelling of the fast pyrolysis of biomass in

5    fluidised bed reactors, Part A: Eulerian computation of momentum transport in bubbling fluidised

6    beds. *Chemical Engineering Science* **2008,** 63, (16), 4218-4227.

7    22.    Xue, Q.; Dalluge, D.; Heindel, T.; Fox, R.; Brown, R., Experimental validation and CFD

8    modeling study of biomass fast pyrolysis in fluidized-bed reactors. *Fuel* **2012,** 97, 757-769.

9    23.    Xiong, Q.; Kong, S.-C.; Passalacqua, A., Development of a generalized numerical

10   framework for simulating biomass fast pyrolysis in fluidized-bed reactors. *Chemical Engineering*

11   *Science* **2013,** 99, 305-313.

12   24.    Papadikis, K.; Bridgwater, A. V.; Gu, S., CFD modelling of the fastpyrolysis of biomass

13   influidised bed reactors, Part A: Eulerian computation of momentum transport in bubbling

14   fluidised beds. *Chemical Engineering Science* **2008,** 63, 4218-4227.

15   25.    Shafizadeh, F.; Bradbury, A., Thermal degradation of cellulose in air and nitrogen at low

16   temperatures. *Journal of Applied Polymer Science* **1979,** 23, (5), 1431-1442.

17   26.    Boateng, A. A.; Mtui, P. L., CFD modeling of space-time evolution of fast pyrolysis

18   products in a bench-scale fluidized-bed reactor. *Applied Thermal Engineering* **2012,** 33-34, 190-

19   198.

20   27.    Varhegyi, G.; Antal Jr, M. J.; Jakab, E.; Szabó, P., Kinetic modeling of biomass pyrolysis.

21   *Journal of analytical and Applied Pyrolysis* **1997,** 42, (1), 73-87.

22   28.    Miller, R.; Bellan, J., A generalized biomass pyrolysis model based on superimposed

23   cellulose, hemicelluloseand liqnin kinetics. *Combustion science and technology* **1997,** 126, (1-6),

24   97-137.

29. Mellin, P.; Zhang, Q.; Kantarelis, E.; Yang, W., An Euler–Euler approach to modeling biomass fast pyrolysis in fluidized-bed reactors – Focusing on the gas phase. *Applied Thermal Engineering* **2013,** 58, (1-2), 344-353.

30. Mellin, P.; Kantarelis, E.; Zhou, C.; Yang, W., Simulation of bed dynamics and primary products from fast pyrolysis of biomass: steam compared to nitrogen as a fluidizing agent. *Industrial & Engineering Chemistry Research* **2014,** 53, (30), 12129-12142.

31. Lédé, J.; Authier, O., Characterization of biomass fast pyrolysis. *Biomass Conversion and Biorefinery* **2011,** 1, (3), 133-147.

32. Debiagi, P. E. A.; Pecchi, C.; Gentile, G.; Frassoldati, A.; Cuoci, A.; Faravelli, T.; Ranzi, E., Extractives extend the applicability of multistep kinetic scheme of biomass pyrolysis. *Energy & Fuels* **2015,** 29, (10), 6544-6555.

33. Kersten, S. R.; Wang, X.; Prins, W.; van Swaaij, W. P., Biomass pyrolysis in a fluidized bed reactor. Part 1: Literature review and model simulations. *Industrial & engineering chemistry research* **2005,** 44, (23), 8773-8785.

34. Zhang, H.; Xiao, R.; Wang, D.; Zhong, Z.; Song, M.; Pan, Q.; He, G., Catalytic fast pyrolysis of biomass in a fluidized bed with fresh and spent fluidized catalytic cracking (FCC) catalysts. *Energy & Fuels* **2009,** 23, (12), 6199-6206.

35. Venderbosch, R.; Prins, W., Fast pyrolysis technology development. *Biofuels, bioproducts and biorefining* **2010,** 4, (2), 178-208.

36. Piskorz, J.; Majerski, P.; Radlein, D.; Scott, D. S.; Bridgwater, A., Fast pyrolysis of sweet sorghum and sweet sorghum bagasse. *Journal of Analytical and Applied Pyrolysis* **1998,** 46, (1), 15-29.

37. Dvornikov, N.; Belousov, P., Investigation of a fluidized bed in a vortex chamber. *Journal of applied mechanics and technical physics* **2011,** 52, (2), 206-211.

56

1    38.    De Wilde, J., Gas–solid fluidized beds in vortex chambers. *Chemical Engineering and*

2    *Processing: Process Intensification* **2014,** 85, 256-290.

3    39.    Eliaers, P.; De Wilde, J., Drying of Biomass Particles: Experimental Study and

4    Comparison of the Performance of a Conventional Fluidized Bed and a Rotating Fluidized Bed in

5    a Static Geometry. *Drying Technology* **2013,** 31, (2), 236-245.

6    40.    Eliaers, P.; Ranjan Pati, J.; Dutta, S.; De Wilde, J., Modeling and simulation of biomass

7    drying in vortex chambers. *Chemical Engineering Science* **2015,** 123, 648-664.

8    41.    Ashcraft, R. W.; Heynderickx, G. J.; Marin, G. B., Modeling fast biomass pyrolysis in a

9    gas–solid vortex reactor. *Chemical Engineering Journal* **2012,** 207-208, 195-208.

10   42.    Ashcraft, R. W.; Kovacevic, J.; Heynderickx, G. J.; Marin, G. B., Assessment of a Gas–

11   Solid Vortex Reactor for SO2/NOxAdsorption from Flue Gas. *Industrial & Engineering*

12   *Chemistry Research* **2013,** 52, (2), 861-875.

13   43.    Weber, J. M.; Stehle, R. C.; Breault, R. W.; De Wilde, J., Experimental study of the

14   application of rotating fluidized beds to particle separation. *Powder Technology* **2017,** 316, 123-

15   130.

16   44.    Verma, V.; Li, T.; De Wilde, J., Coarse-grained discrete particle simulations of particle

17   segregation in rotating fluidized beds in vortex chambers. *Powder Technology* **2017,** 318, 282-

18   292.

19   45.    Trujillo, W. R.; De Wilde, J., Influence of solids outlets and the gas inlet design on the

20   generation of a gas-solids rotating fluidized bed in a vortex chamber for different types of

21   particles. *Chemical Engineering Science* **2017,** 173, 74-90.

22   46.    Niyogi, K.; Torregrosa, M. M.; Pantzali, M. N.; Heynderickx, G. J.; Marin, G. B.,

23   Experimentally validated numerical study of gas-solid vortex unit hydrodynamics. *Powder*

24   *Technology* **2017,** 305, 794-808.

57

47. Kovacevic, J. Z.; Pantzali, M. N.; Heynderickx, G. J.; Marin, G. B., Bed stability and maximum solids capacity in a Gas–Solid Vortex Reactor: Experimental study. *Chemical Engineering Science* **2014,** 106, 293-303.

48. Niyogi, K.; Torregrosa, M. M.; Shtern, V. N.; Marin, G. B.; Heynderickx, G. J., On the Mechanisms of Secondary Flows in a Gas Vortex Unit. *AIChE Journal* **2018**.

49. Pantzali, M. N.; Kovacevic, J. Z.; Heynderickx, G. J.; Marin, G. B.; Shtern, V. N., Radial pressure profiles in a cold□flow gas□solid vortex reactor. *AIChE Journal* **2015,** 61, (12), 4114-4125.

50. Friedle, M.; Niyogi, K.; Torregrosa, M. M.; Marin, G. B.; Heynderickx, G. J., A drag model for the gas-solid vortex unit. *Powder Technology* **2017,** 312, 210-221.

51. Gonzalez-Quiroga, A.; Reyniers, P. A.; Kulkarni, S. R.; Torregrosa, M. M.; Perreault, P.; Heynderickx, G. J.; Van Geem, K. M.; Marin, G. B., Design and cold flow testing of a Gas-Solid Vortex Reactor demonstration unit for biomass fast pyrolysis. *Chemical Engineering Journal* **2017,** 329, 198-210.

52. Kovacevic, J. Z.; Pantzali, M. N.; Niyogi, K.; Deen, N. G.; Heynderickx, G. J.; Marin, G. B., Solids velocity fields in a cold-flow gas–solid vortex reactor. *Chemical Engineering Science* **2015,** 123, 220-230.

53. Menter, F. R., Two-equation eddy-viscosity turbulence models for engineering applications. *AIAA journal* **1994,** 32, (8), 1598-1605.

54. Jenkins, J. T.; Savage, S. B., A theory for the rapid flow of identical, smooth, nearly elastic, spherical particles. *Journal of fluid mechanics* **1983,** 130, 187-202.

55. Gidaspow, D., *Multiphase flow and fluidization: continuum and kinetic theory descriptions*. Academic press: 1994.

58

1  56.    Ranzi, E.; Cuoci, A.; Faravelli, T.; Frassoldati, A.; Migliavacca, G.; Pierucci, S.;

2  Sommariva, S., Chemical Kinetics of Biomass Pyrolysis. *Energy & Fuels* **2008,** 22, (6), 4292-

3  4300.

4  57.    Guizani, C.; Valin, S.; Billaud, J.; Peyrot, M.; Salvador, S., Biomass fast pyrolysis in a

5  drop tube reactor for bio oil production: Experiments and modeling. *Fuel* **2017,** 207, 71-84.

6  58.    Lehmann, J.; Joseph, S., *Biochar for Environmental Management: Science and*

7  *Technology*. Earthscan: 2012.

8  59.    Via, B.; Fasina, O.; Pan, H., Assessment of pine biomass density through mid-infrared

9  spectroscopy and multivariate modeling. *BioResources* **2013**.

10  60.    Di Blasi, C., Modelling the fast pyrolysis of cellulosic particles in fluid-bed reactors.

11  *Chemical Engineering Science* **2000,** 55, (24), 5999-6013.

12  61.    Guedes, R. E.; Luna, A. S.; Torres, A. R., Operating parameters for bio-oil production in

13  biomass pyrolysis: A review. *Journal of Analytical and Applied Pyrolysis* **2017**.

14  62.    Zhou, Z.; Yu, A.; Zulli, P., Particle scale study of heat transfer in packed and bubbling

15  fluidized beds. *AIChE Journal* **2009,** 55, (4), 868-884.

16  63.    Ma, Y.; Zhu, J.-X., Experimental study of heat transfer in a co-current downflow

17  fluidized bed (downer). *Chemical Engineering Science* **1999,** 54, (1), 41-50.

18  64.    Grace, J. R. In *Heat transfer in circulating fluidized beds*, Circulating Fluidized Bed

19  Technology: Proceedings of the First International Conference, 1986; Elsevier: 1986; pp 63-81.

20  65.    Ding, J.; Gidaspow, D., A bubbling fluidization model using kinetic theory of granular

21  flow. *AIChE Journal* **1990,** 36, (4), 523-538.

22  66.    Gidaspow, D.; Bezburuah, R.; Ding, J. *Hydrodynamics of circulating fluidized beds:*

23  *kinetic theory approach*; Illinois Inst. of Tech., Chicago, IL (United States). Dept. of Chemical

24  Engineering: 1991.

1    67.    Syamlal, M.; Rogers, W.; OBrien, T. J. *MFIX documentation theory guide*; USDOE

2    Morgantown Energy Technology Center, WV (United States): 1993.

3    68.    Schaeffer, D. G., Instability in the evolution equations describing incompressible granular

4    flow. *Journal of differential equations* **1987,** 66, (1), 19-50.

5    69.    Lun, C.; Savage, S. B.; Jeffrey, D.; Chepurniy, N., Kinetic theories for granular flow:

6    inelastic particles in Couette flow and slightly inelastic particles in a general flowfield. *Journal of*

7    *fluid mechanics* **1984,** 140, 223-256.

8    70.    Johnson, P. C.; Jackson, R., Frictional–collisional constitutive relations for granular

9    materials, with application to plane shearing. *Journal of fluid Mechanics* **1987,** 176, 67-93.

10    71.    Gunn, D.; De Souza, J., Heat transfer and axial dispersion in packed beds. *Chemical*

11    *Engineering Science* **1974,** 29, (6), 1363-1371.

12    72.    Scheer, A. M.; Mukarakate, C.; Robichaud, D. J.; Nimlos, M. R.; Carstensen, H.-H.;

13    Barney Ellison, G., Unimolecular thermal decomposition of phenol and d5-phenol: Direct

14    observation of cyclopentadiene formation via cyclohexadienone. *The Journal of chemical physics*

15    **2012,** 136, (4), 044309.

16    73.    Vinu, R.; Broadbelt, L. J., A mechanistic model of fast pyrolysis of glucose-based

17    carbohydrates to predict bio-oil composition. *Energy & Environmental Science* **2012,** 5, (12),

18    9808-9826.

19    74.    Paulsen, A. D.; Mettler, M. S.; Dauenhauer, P. J., The role of sample dimension and

20    temperature in cellulose pyrolysis. *Energy & Fuels* **2013,** 27, (4), 2126-2134.

21